SELECTIVE STRONG-FIELD ENHANCEMENT AND ATTENUATION OF EXCITATION AND IONIZATION WITH SHORT LASER PULSES

A Dissertation

by

NATHAN ANDREW HART

Submitted to the Office of Graduate and Professional Studies of
Texas A&M University
in partial fulfillment of the requirements for the degree of

DOCTOR OF PHILOSOPHY

Chair of Committee,	Hans Schuessler
Committee Members,	George Kattawar
	Aleksei Zheltikov
	Andrea Bonito
Head of Department,	George Welch

May 2015

Major Subject: Physics

ABSTRACT

The coherent control of atomic energy level population is important for several areas physics and engineering including fluorescent spectroscopy, resonantly enhanced multiphoton ionization, harmonic generation, remote sensing and lasing. At low intensities where the Stark shift can be neglected, coherent control mechanisms usually exploit resonances created from stationary energy states dressed by integer multiples of the photon energy. However, in the strong field limit where large laser pulse intensities lead to significant Stark shifts, the resonant conditions are dynamic both in time and space and will likely not be satisfied for the entire laser pulse or beam.

In this research, we experimentally and theoretically demonstrate coherent control of atomic energy level population in sodium vapor as well as the selective excitation of sodium Rydberg levels using high intensity laser pulses. We also make a direct measurement of the ponderomotive shift of the continuum. While techniques based on resonance interferences and rapid adiabatic passage have been introduced for selective excitation, the conditions that must be satisfied for these phenomena can be hampered by short femtosecond pulse durations and large Stark shifts. In contrast, a technique referred to here as Resonance Sampling, uses the AC Stark shifts to selectively induce Freeman resonances and is resilient to changes in the spectral phase. Freeman resonances established in this way can result in population inversion of the excited state, and may lead to new lasing mediums and remote sensing applications.

DEDICATION

"And what do you benefit if you gain the whole world but lose your own soul? Is anything worth more than your soul?" Matthew 16:26 (Jesus of Nazareth)

"If I give everything I own to the poor and even go to the stake to be burned as a martyr, but I don't love, I've gotten nowhere. So, no matter what I say, what I believe, and what I do, I'm bankrupt without love.

Love never gives up. Love cares more for others than for self. Love doesn't want what it doesn't have. Love doesn't strut, Doesn't have a swelled head, Doesn't force itself on others, Isn't always "me first," Doesn't fly off the handle, Doesn't keep score of the sins of others, Doesn't revel when others grovel, Takes pleasure in the flowering of truth, Puts up with anything, Trusts God always, Always looks for the best, Never looks back, But keeps going to the end." 1 Corinthians 13:3-7 (Paul of Tarsus)

ACKNOWLEDGEMENTS

I would like to thank my advisor Hans Schuessler for making this research possible, for helping to guide my research topics and for giving my experiments priority. I would like to thank Dr. James Strohaber for detailed and critically constructive discussions and for teaching me how to take experimental data. Additionally, I would like to thank Alexandre Kolomenski, for asking good questions and guiding the completion of this dissertation. I would like to thank Gerhard Paulus for allowing me to use his stereo ATI machine and some computer codes. I would also like to thank Dieter Bauer for his help and discussions related to potential applications of my research. To my committee members, George Kattawar, Aleksei Zheltikov and Andrea Bonito, I am grateful for all your time and help.

I acknowledge the Department of Physics at Texas A&M University for their financial support over the past few years and the Office of Graduate and Professional Studies for awarding me the 2015 Dissertation Fellowship.

It has been a privilege to work in the Attosecond and Fewcycle Laser Laboratory with Feng Zhu, Necati Kaya, Gamze Kaya, Muhammed Sayrac, Ruqayyah F. Askar, Yakup Boran, Aysenur Bicer, and Sunilkumar Anumula.

I would like to thank my ReJOYce IN JESUS family for their prayers. And finally, a special thanks goes to my mother, father and sister for their prayers, advice, encouragement and support. I love you guys!

TABLE OF CONTENTS

Page

LIST OF FIGURES

Page

1. INTRODUCTION

In the presence of high laser intensities, AC Stark shifts and optical dispersion can lead to excitation dynamics which are hard to predict from perturbation theory or solving the time dependent Schrodinger equation (TDSE) numerically. In this dissertation, I present ultra-short pulse experiments of above threshold ionization (ATI) in sodium vapor which survey the parameter space of laser peak intensity, frequency composition and dispersion in the strong field regime (intensity, $I_0 > 10^{12}$ W/cm^2). We experimentally demonstrate both selective enhancement and attenuation of energy level excitation with high intensity pulses. This manipulation of the population allows us to coherently control the resonantly enhanced multiphoton ionization (REMPI) of the atom. It is shown that the dominant means of coherent control can be explained by incorporating the dynamic detuning into a multiphoton perturbative model referred to here as Resonance Sampling (RS). To describe the data, this simple model does not require quantum interference effects such as Rabi oscillations, adiabatic passage, dual path interference, or Feynman path interferences. Therefore, the model presents an elegant interpretation of highly non-linear and analytically intractable ionization phenomena. This is important because the resonant ionization of atoms and molecules has recently become an area of immense importance in several areas of physics and engineering such as high harmonic generation (HHG), plasma physics, and remote sensing. The reason being that, resonant excitation of the atom prior to ionization can increase the efficiency of this process by orders of magnitude[1-3].

An important feature of multiphoton ionization is that if there is a dipole allowed transition near a multiphoton resonance, abnormal intensity and wavelength dependences in the excitation develop which depart from the expected multiphoton absorption predicted by perturbation theory. In the analysis of multiphoton ionization, the parameter $K \equiv Log(W)/Log(I)$ is an important measure of nonlinear excitation, where W is the excitation rate, I is the laser intensity and thus $W \propto I^K$. For an electronic transition requiring at least N photons, perturbation theory predicts that the photon absorption rate is proportional to the intensity to the N^{th} power (K = N). However, using Cesium (Cs) atoms, B. Held *et. al.*[4] showed experimentally and C. S. Chang and P. Stehle[5] demonstrated theoretically that a 4 photon ionization could have a K value as low as 1 and as high as 8 depending on the amount of detuning from the resonance. In their experiment, they measured the Cs ion yield for different laser wavelengths at a constant intensity $I_0 = 1.4 \times 10^8 \mathrm{W/cm^2}$. This procedure effectively sampled the 3 photon detuning between the 6s ground state and the 6f excited state (6s$\rightarrow\rightarrow\rightarrow|\Delta|6f$). They also noticed that the maximum ionization rate occurred when the detuning was slightly above the resonance, indicating that the AC Stark shift of *6f* changed the effective detuning. Mittleman[6] points out that the K = 1 case can be explained by the saturation of the Rydberg state early in the laser pulse. If the population probability of *6f* approached unity during the rise of the laser field, *6f* becomes an effective ground state of Cs, and only one photon is needed to further ionize at the pulse's peak.

A pivotal breakthrough occurred when Freeman *et. al.*[1] discovered that when atomic Rydberg states Stark-shift into resonance, they may be spectrally/energetically resolved

in the electron yield. Observation of the ionized electron energy spectra requires the pulse duration to be shorter than the time it takes for ionized electrons to exit the laser focus and requires that the laser bandwidth be smaller than the spacing between the excited energy levels. This dynamic shift into resonance is commonly referred to as a "Freeman resonance" and is a pervasive phenomenon in strong field physics partly because it satisfies the condition for REMPI. Therefore, Freeman resonances are generally associated with enhanced coherent ionization[7].

Freeman resonances of bound atomic states very near the continuum (channel closing) can lead to an enhancement of HHG[8,9] beyond that observed through the tunneling ionization model of Corkum[10]. At the channel closing, bound Rydberg states with near zero energy Stark shift into an integer photon resonance ($n\hbar\nu$). Electrons occupying these high lying states have energies approaching those of an electron tunneling through the potential barrier. The relatively high efficiency of the resonant transition leads to a higher density of atoms with near zero electron energy and higher HHG output.

REMPI has been exploited to create air lasing at remote distances[11,12]. With this approach, a 226nm wavelength pump pulse disassociates O2 with a 2+1 REMPI leaving O+ and a neutral oxygen atom. The same pump pulse excites the neutral oxygen to an excited level 3*p* while a 845nm Stokes pulse prepares the population inversion in the 3*s* state. Oxygen atoms are excited along the Rayleigh range, and spontaneous emission initiates lasing to the ground state both in the forward and backward direction.

Radar REMPI is a relatively new technique for the remote detection of atomic and molecular species[13]. For this technique, a coherently controlled laser pulse is focused at a remote location to selectively ionize atoms or molecules of interest through intermediate resonant transitions. Then a radar pulse is sent to scatter off the newly created ions in proportion to the ion density. An increase in the scattering signals a positive detection. Radar REMPI is being utilized for flame analysis to test the efficiency of combustion in systems such as jet engines[13] and is currently being investigated for the detection of chemical explosives[13]. As the applied uses for REMPI expand, there is increasing demand for robust coherent control methods using short pulses with high intensities.

Strong field coherent control was birthed by the discovery that at sufficiently high intensity, energy levels that are far detuned from an integer photon resonance and lie outside of the bandwidth of the laser can be significantly populated and enhance ATI through the Autler-Towns (Rabi splitting) effect[14-17]. Moreover, it was shown that the split levels could be asymmetrically populated leading to energy selectivity[18].

C. Trallero-Herrero and company performed a detailed theoretical study of coherent control in the strong field limit using a single femtosecond pulse[19-21]. Through simulations, they found optimum phase parameters for efficient excitation of two and three level ladder systems by surveying the parameter space of the spectral phase. One key insight was that by making the time-dependent Stark shift follow the instantaneous frequency, a multiphoton π pulse could be created to transfer ~100% of the population to the excited state. In other words, by shaping the pulse, they could cancel the relative shift of the excited state with respect to the instantaneous laser frequency such that a

constant detuning from resonance is maintained throughout the pulse duration. Moreover, the authors provided rules of thumb for obtaining efficient transfer in a two level system using Fourier-transform limited pulses[20].

While custom pulse shaping using genetic algorithms has shown selective excitation[19-23], M Krug, et. al.[24] demonstrated that 3 photon excitation could be controlled by the intensity and phase chirp parameters alone. In general, there are two types of atom-photon population transfer: sequential and non-sequential (direct). Sequential excitation requires that an electron promoted from the ground state to a final energy level occupies an intermediate resonance during the population transfer. While with direct excitation, the final state is populated without the excitation of an intermediate state. Sangkyung Lee, et. al.[25] performed detailed analysis of these pathways and the interference that they produce. Theory and experiment confirmed that the sequential path contributes the dominant portion of the excitation in a dynamic Stark shift environment.

In this dissertation, we make the first direct measurement of the ponderomotive shift, demonstrate robust selective excitation and present a qualitative model for predicting the population dynamics of atoms. The RS model presented in this work explains the results of strong field coherent control currently and is of utility in the understanding of REMPI.

2. EXPERIMENTAL SETUP

A Ti:sapphire laser oscillator outputs 20-fs modelocked laser pulses with a center wavelength of 800 nm and a repetition rate of 80 MHz. The oscillator provides seed pulses to a Spectra Physics TSA Spitfire regenerative laser amplifier which uses the Chirped Pulse Amplification (CPA) technique to produce 57 fs pulses. In the CPA technique, the stretcher (STR) temporally lengthens the pulse to lower the peak intensity and protect the Ti:sapphire crystal during the amplification stage. Then a single pulse from the 80 MHz train is amplified every millisecond. And finally, the amplified pulse is temporally shortened in the grating compressor (GC). The desired chirp of the pulse for the experiment is made by adjusting the position of the grating compressor in the laser amplifier. The position of the GC was measure by a Mitutoyo digital indicator. A 4nm portion of the seed pulse spectrum was attenuated using a thin piece of metal vertically fixed to a Newport ESP301 translation stage (TS). The pulse duration was measured after the GC by frequency resolved optical gating using a GRENOUILLE 8-20 by Swamp Optics, LLC. The output pulses had a central wavelength of 800 nm, a1 kHz repetition rate and were approximately 0.9 mJ in energy.

Since shorter pulses have a higher peak intensity for a given pulse energy, temporal compression of the laser pulses in the focus was achieved by maximizing the integrated photoelectron yield in the ATI apparatus with adjustments to the GC. A photodiode (PD) detects the laser pulses before the half-wave plate (WP) of the attenuator and triggers the data-acquisition software (see Figure 1). The attenuator was a two component device composed of a rotatable half-wave plate that changes the polarization of the laser beam

and a fixed polarizing beam-splitter cube (PBC) that filtered out vertically polarized radiation while passing the horizontal polarization.

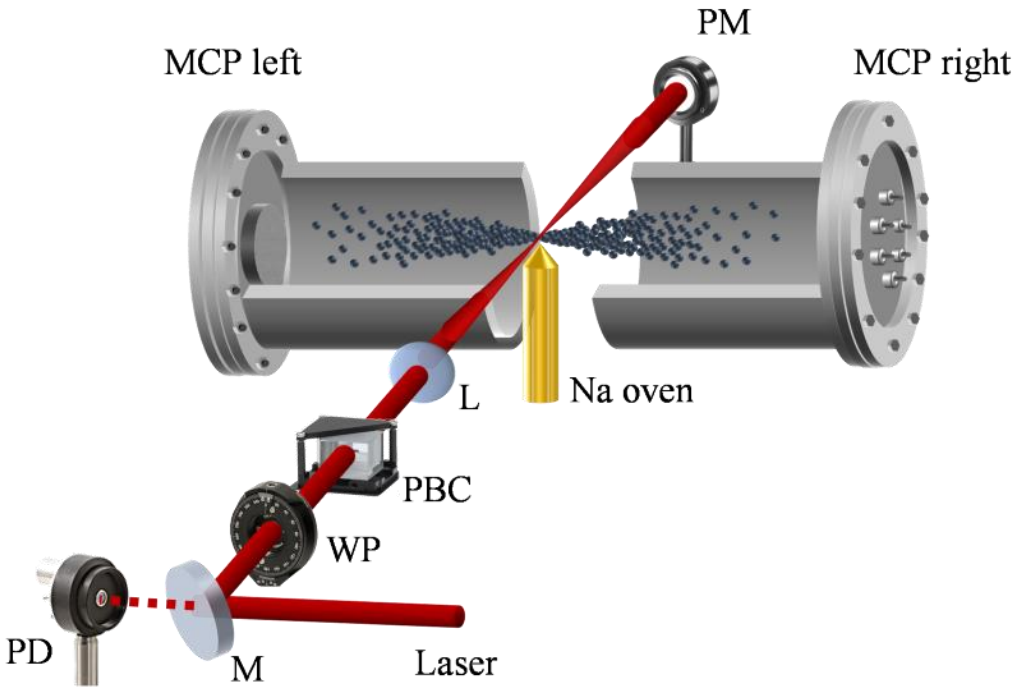

Figure 1. The experimental apparatus and associated optics. The laser is steered into the apparatus by steering mirrors.

The orientation of the wave plate was automated to rotate such that the desired laser power was achieved after the polarizing cube. The spectral content of the femtosecond pulse was measure by a spectrometer (SM) from a piece of paper scattering the filtered vertically polarized beam. A 20 cm achromatic lens (L) focused the beam to the center of the vacuum chamber where the sodium oven (Na oven) sat ~1.5 cm below the laser focal point. The sodium atoms and dimers diffuse from the oven into the chamber according to the Lambert's Cosine Law. The oven temperature was maintained at 256 C

which created a Na vapor density of 1.98×10^{14} cm^{-3} at the exit of the oven and a density of 5.17×10^{13} cm^{-3} at the laser focus.

Laser ionized electrons that travel down the μ-metal tube in the direction of the electric field are detected at the microchannel plate (MCP). The MCP signal was amplified by a high bandwidth Mini-Circuits ZKL-2 preamplifier before being registered by a pulse counter (MS) with 100 ps timing resolution. The average laser power was measured after the beam exits the vacuum chamber by a power meter (PM).

All experiments were automated using National Instruments (NI) DAQ PCI-MIO-16E-4 card, NI BNC 2090 box and custom NI LabView programs and. The following components were automated by Labview sub-VI's and incorporated into a Labview VI program that controlled the entire experiment and data collection:

- Newport ESP301(TS)
- New Focus translation stage (GC)
- Mitutoyo IT007R and Mitutoyo Digimatic Indicator ID-C
- New Focus Pico Diver and New Focus Pico Rotator (the holder for WP)
- Ocean Optics USB2000 (SM)
- OPHIR NOVA II (PM)
- FAST ComTec MCS6 multiscaler (MS)

3. CHARACTERISTICS OF A LASER PULSE

3.1 Gaussian Beam Geometry

A Gaussian beam has a spatial profile that is radially symmetric in cylindrical coordinates. The electric field amplitude and intensity as a function of the radial and longitudinal variables r and z respectively:

$$\mathcal{E}(r,z) = \mathcal{E}_0 \left(\frac{w_0}{w(z)}\right) e^{-\frac{r^2}{w^2(z)}} \tag{3.1}$$

$$I(r,z) = I_0 \left(\frac{w_0}{w(z)}\right)^2 e^{-\frac{2r^2}{w^2(z)}} \tag{3.2}$$

where w_0 is the beam waist, $w(z) = w_0\sqrt{1+\left(\frac{z}{z_R}\right)^2}$ and $z_R = \frac{\pi w_0^2}{\lambda}$. This is referred to as the fundamental transverse mode or TEM_{00} mode of a laser beam. Solving for r^2 we get:

$$r(I,I_0,z)^2 = w^2(z)\ln\left[\frac{I_0}{I}\frac{w_0^2}{w^2(z)}\right] \tag{3.3}$$

The radius $r = 0$ when the argument $\frac{I_0}{I}\frac{w_0^2}{w^2(z)} = 1$, or $z_\pm \equiv \pm z_R\left(\frac{I_0}{I}-1\right)$. Using equation 3.3, the three-dimensional volume of a laser beam with peak intensity I_0 bounded by an intensity I is:

$$V_3(I,I_0) = \pi\int_{z_-}^{z_+} r^2(I,I_0,z)dz \tag{3.4}$$

$$= \pi z_R w_0^2\left\{\frac{4}{3}\left[\frac{I_0}{I}-1\right]^{\frac{1}{2}} + \frac{2}{9}\left[\frac{I_0}{I}-1\right]^{\frac{3}{2}} - \frac{4}{3}\arctan\left[\frac{I_0}{I}-1\right]^{\frac{1}{2}}\right\} \tag{3.5}$$

For two dimensions a cross-sectional slice of the laser gives a disk like volume bounded by an intensity I.

$$V_2(I, I_0) = \pi\, r^2(I, I_0, z)\Delta z \tag{3.6}$$

The one dimensional differential volume is merely a rod along the y axis intersecting the x and z axis of the laser.

$$V_1(I, I_0) = 2r(I, I_0, z)\, \Delta x\, \Delta z \tag{3.7}$$

The space between radii $r(I_i, I_0, z)$ and $r(I_{i+1}, I_0, z)$ for some intensities $I_{i+1} < I_i < I_0$ define an iso-intensity shell confined by I_i and I_{i+1}(see Figure 2).

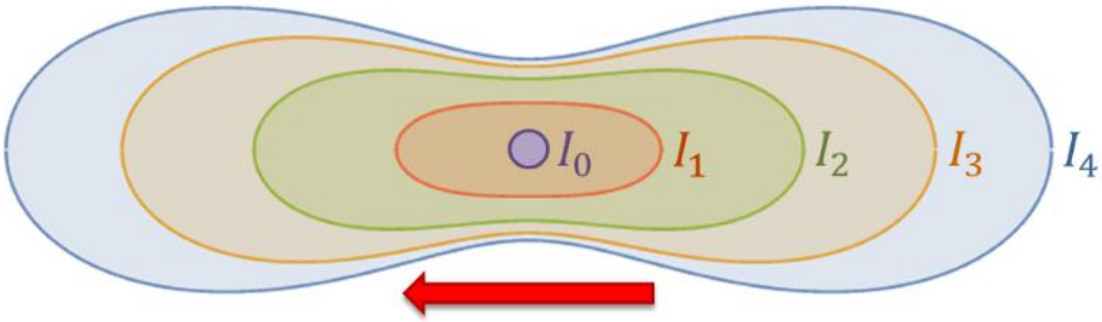

Figure 2. A depiction of the two-dimensional iso-intensity shells. The laser z-axis is along the red arrow. The peak intensity I_0 is at the center of the volume and has an essentially zero volume. Each iso-intensity shell is represented by a thin, closed curve with an intensity of I_i enclosing all intensities greater than I_i up to I_0. Note that $I_0 > I_1 > I_2 > I_3 > I_4$.

3.2 Chirped Pulse and Second Order Dispersion

To understand how a laser pulse interacts with matter it is important to characterize the time dependence of its electric field. A pulse describes to the temporal characteristics of a lasers electric field, analogous to the spatial information for the same field that beam refers to. Here we will describe a pulse whose electric has a temporal Gaussian envelope. Since Gaussian functions taper off asymptotically as their argument tends to positive or negative infinity, there is no clear cutoff for a Gaussian pulse. Therefore, it is

convenient and customary to define the pulses duration τ as the full width of the pulse measured at half its peak intensity value. We will continue to use this convention, termed full-width-half-max (FWHM), for the entirety of this dissertation. The electric field is expressed as:

$$\mathcal{E}(t) = \sqrt{\frac{\tau_0}{\tau}}\mathcal{E}_t e^{-2Log(2)\left(\frac{t}{\tau}\right)^2} Cos\left(\nu_0 t + \frac{\alpha}{2}t^2\right) \tag{3.8}$$

or more generally as:

$$\mathcal{E}(t) = \sqrt{\frac{\tau_0}{\tau}}\mathcal{E}_t e^{-2Log(2)\left(\frac{t}{\tau}\right)^2} e^{i\left(\nu_0 t + \frac{\alpha}{2}t^2\right)} \tag{3.9}$$

where $\mathcal{E}_t$ is the constant peak electric field, the factor 2*Ln*(2) comes from the FWHM definition of the pulse duration τ, ν_0 is the average frequency of the laser, α is the second order chirp parameter and τ_0 is the pulse duration evaluated when α = 0. The pulse duration τ increases with the magnitude of the chirp α. Therefore, the factor $\sqrt{\tau_0/\tau}$ in front of $\mathcal{E}_0$ is needed to conserve the pulse energy. This fact can be verified by integrating the intensity ($\propto |\mathcal{E}(t)|^2$), derived from Eq. 3.9, with respect to time from -∞ ≤ *t* ≤ ∞ and requiring the integral to be constant. The instantaneous frequency ν(*t*) can be found by taking the time derivative of the argument in the sinusoidal function.

$$\nu(t) = \frac{d}{dt}\left(\nu_0 t + \frac{\alpha}{2}t^2\right) = \nu_0 + \alpha t \tag{3.10}$$

More details about the chirp parameter α and the pulse duration τ will be discussed later in this section. We can check that (3.9) satisfies the FWHM condition by noting that the intensity:

$$
\begin{aligned}
I\left(\frac{\tau}{2}\right) &= \frac{\epsilon_0 c}{2}\frac{\tau_0}{\tau}\left|\mathcal{E}\left(\frac{\tau}{2}\right)\right|^2 \\
&\approx \frac{\epsilon_0 c}{2}\frac{\tau_0}{\tau}\left|\mathcal{E}_0\right|^2 e^{-4Ln(2)\left(\frac{\tau}{2\tau}\right)^2} \\
&= \frac{\epsilon_0 c}{2}\frac{\tau_0}{\tau}\left|\mathcal{E}_0\right|^2\left(\frac{1}{2}\right) \\
&= I_0\left(\frac{1}{2}\right)
\end{aligned}
\tag{3.11}
$$

The spectrum of the laser pulse can be found by taking a normalized Fourier transform of the electric field $\mathcal{E}(t)$ (Eq. 3.8):

$$
\begin{aligned}
\mathcal{E}(\omega) &= \frac{1}{\sqrt{2\pi}}\sqrt{\frac{\tau_0}{\tau}}\int_{-\infty}^{\infty}\mathcal{E}(t)e^{-i\omega t}dt \\
&\approx \frac{1}{\sqrt{2\pi}}\sqrt{\frac{\tau_0}{\tau}}\int_{-\infty}^{\infty}\mathcal{E}_0 e^{-2Ln(2)\left(\frac{t}{\tau}\right)^2}\left(\frac{e^{i\left(\nu_0 t+\frac{\alpha}{2}t^2\right)}}{2}\right)e^{-i\omega t}dt \qquad (3.12) \\
&\approx \mathcal{E}_\omega Exp\left(-\frac{(\omega-\nu_0)^2\tau_0^2}{8Ln(2)} - i\varphi''\frac{(\omega-\nu_0)^2}{2}\right) \qquad (3.13)
\end{aligned}
$$

where,

$$
\varphi'' = \left(\frac{\alpha\tau_0^4}{16Ln(2)^2}\right)\left(\frac{1}{1+\frac{\alpha^2\tau_0^4}{16Ln(2)^2}}\right) \tag{3.14}
$$

is the second order dispersion (SOD) or group delay dispersion (GDD) with units of [s^2]. The significance of Eq. 3.14 is that it allows one to calculate the chirp α/2 given a measured SOD φ'' from a pulse characterizing instrument such as a GRENOUILLE (by Swamp Optics, LLC) or vice versa. The constant electric field amplitude in the frequency domain is given by

$$\mathcal{E}_{\omega} = \sqrt{\frac{1}{2}\left(\frac{\frac{2Ln(2)}{\tau^2} + i\frac{\alpha}{2}}{\left(\frac{2Ln(2)}{\tau^2}\right)^2 + \left(\frac{\alpha}{2}\right)^2}\right)} \sim \frac{\tau}{\sqrt{4Ln(2)}} \tag{3.15}$$

The spectral bandwidth (FWHM) of the pulse derived from the Eq. 3.13 (squared) is:

$$\Delta\nu = 2\pi\Delta f = \frac{4Ln(2)}{\tau_0} \tag{3.16}$$

which is a statement of the quantum uncertainty principle ($\hbar\Delta\nu\cdot\tau_o/4 = 0.7\hbar \approx \hbar/2$). In Eq. 3.12 we used a rotating wave approximation since:

$$Exp\left(-\frac{(\omega-\nu_0)^2\tau^2}{8Ln(2)}\right) \gg Exp\left(-\frac{(\omega+\nu_0)^2\tau^2}{8Ln(2)}\right) \tag{3.17}$$

and then factored the argument of exponential with respect to time:

$$(-At^2 + Bt + C) - C = -A\left(t - i\sqrt{C/A}\right)^2 - C \tag{3.18}$$

for

$$A = \left(\frac{2Ln(2)}{\tau^2} - \frac{i\alpha}{2}\right) \tag{3.19}$$

$$B = i(\nu_0 - \omega) \tag{3.20}$$

$$C = -\frac{B^2}{2\sqrt{A}} \tag{3.21}$$

before performing the integration.

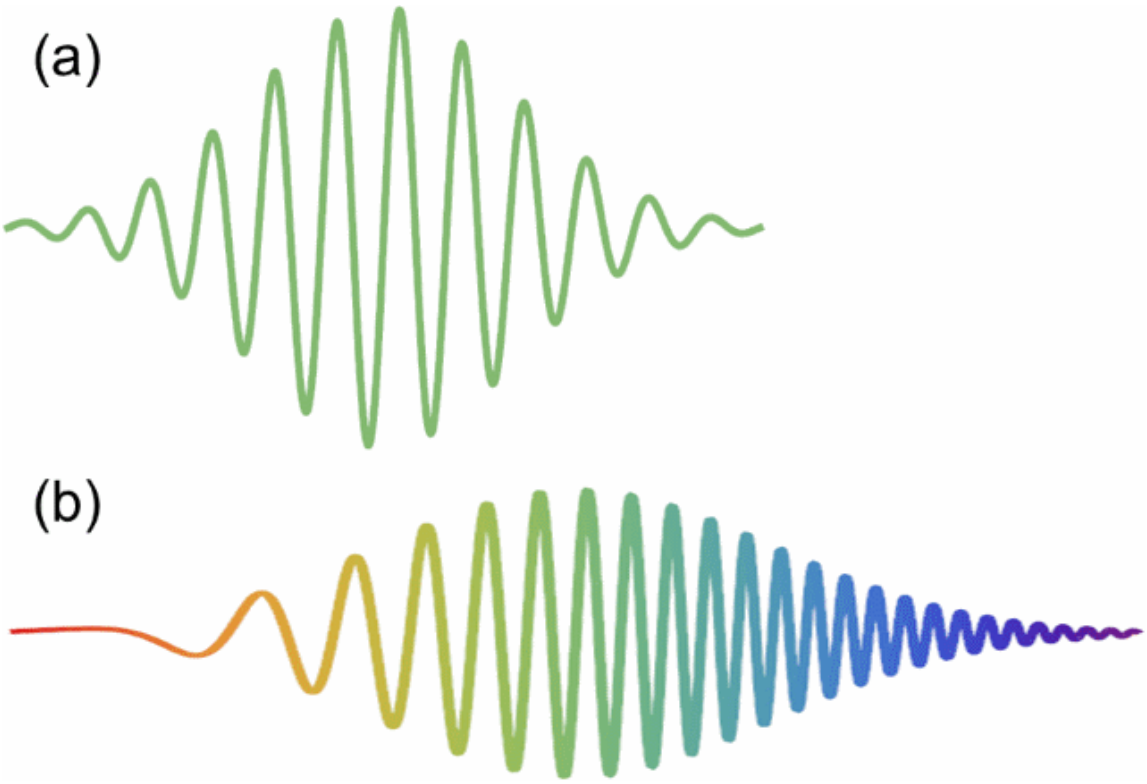

Figure 3. (a) An unchirped Gaussian pulse. (b) A chirped pulse with a reduced amplitude and time dependent frequency. The relative amplitude $\mathcal{E}_t$, pulse duration τ and frequencies $\nu(t)$ of pulses (a) and (b) have been graphically exaggerated for effect and are not to scale.

Second order dispersion can greatly affect nonlinear optical phenomena through not only phase modification but also by increasing the pulse duration along with a simultaneous decrease in the electric field amplitude (see

Figure **3**). Therefore, it is important to find τ as a function of $\boldsymbol{\varphi''}$. This can be accomplished by Fourier transforming the spectrum Eq. 3.13 back into the time domain and comparing the result to Eq. 3.9. Hence, we have a pulse duration of

$$\tau = \tau_0 \sqrt{1 + \left(\frac{4Ln(2)\varphi''}{\tau_0^2}\right)^2}. \tag{3.22}$$

3.3 Multiphoton Pulse Duration and Bandwidth

Fermi's Golden rule may be used to calculate the one photon transition rate between two atomic energy states in the presence of a driving field. The probability amplitude for the transition is proportional to the lasers electric field. However, it is known that the amplitude *A* of a multiphoton transition per unit time is proportional to the electric field of the laser to the n^{th} power,

$$\begin{aligned} A &\propto \mathcal{E}(t)^n \\ &\propto \mathcal{E}_0 e^{-n\left(2Log(2)\left(\frac{t}{\tau}\right)^2\right)} e^{in\left(\nu_0 t+\frac{\alpha}{2}t^2\right)} \end{aligned} \tag{3.23}$$

where *n* is the multiphoton order (or number of photons required for the transition)[26]. Note that this implies an effective *multiphoton pulse duration*,

$$\tau_n = \tau/\sqrt{n} \tag{3.24}$$

where,

$$A \propto \mathcal{E}_0 e^{-2Log(2)\left(\frac{t}{\tau_n}\right)^2} e^{in\left(\nu_0 t+\frac{\alpha}{2}t^2\right)}. \tag{3.25}$$

By the quantum uncertainty relation, Eq. 3.16 shows us that the *multiphoton bandwidth* is

$$\Delta\nu_n = \sqrt{n}\Delta\nu. \tag{3.26}$$

The multiphoton bandwidth can also be verified by Fourier transforming Eq. 3.25 into the frequency domain and finding the FWHM frequency.

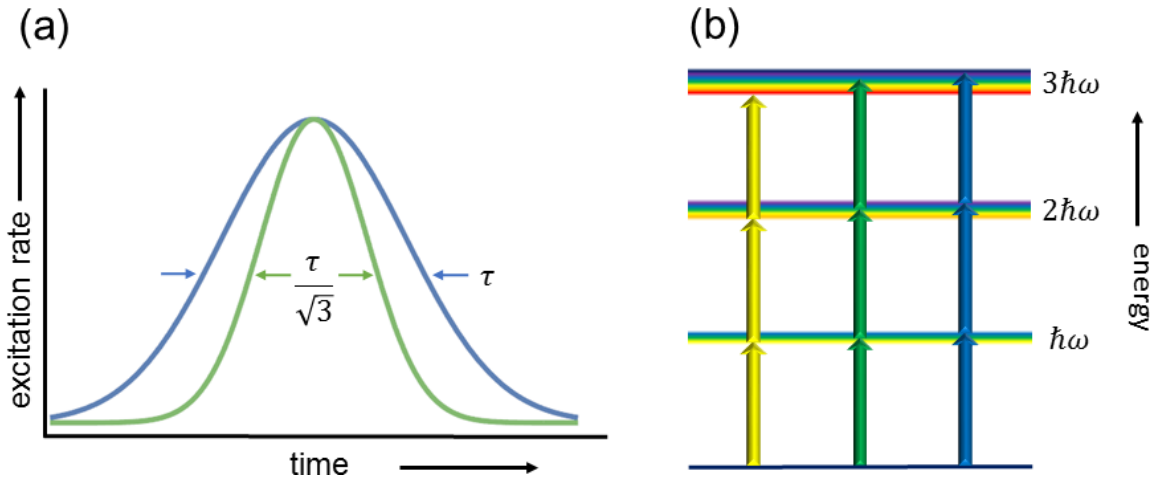

Figure 4. Diagrams comparing the multiphoton pulse duration (left) and the multiphoton bandwidth (right) with the single photon pulse duration and bandwidth respectively. (a) shows a peak-normalized three photon rate in green (inner curve) and a one photon rate in blue. (b) shows the spreading of the bandwidth with each photon order up to $3\hbar\omega$. In contrast to the colors of the photons (yellow, green and blue arrows), the colors in the graphical multiphoton bandwidths, labeled $2\hbar\omega$ and $3\hbar\omega$, should be interpreted as the relative spread in the multiphoton spectrum rather than the actual multiphoton energy.

The implication of this new pulse duration (Eq. 3.24) is that an n^{th} order nonlinear process must on average take place in a window of time that is $1/\sqrt{n}$ shorter than the original pulse (see Figure 4(a)). Moreover, the frequency spread that is accessible to this nonlinear process is $\sqrt{n}$ times larger than the laser pulse bandwidth.

4. THEORY OF LASER-MATTER INTERACTION*

4.1 Rabi Frequency

Atoms in the presence of a laser field have their atomic states perturbed by an interaction Hamiltonian. But before uncovering the effects of this laser induced interaction we must define the Schrodinger equation for the unperturbed atom as:

$$i\hbar\frac{d}{dt} = \widehat{H}_0 \tag{4.1}$$

The eigenvalues of the atomic Hamiltonian operator $\widehat{H}_0$, denoted by $E_j = \hbar\omega_j$, are referred to as the energy levels of the atom, and j labels a specific energy state. The eigenvectors satisfying the Schrodinger equation have the form:

$$|\varphi_j\rangle = |j\rangle e^{-i\omega_j t}, \tag{4.2}$$

and satisfy the orthogonality relations $\langle\varphi_j|\varphi_j\rangle = 1$ and $\langle\varphi_j|\varphi_k\rangle = 0$ for $k \neq j$. The Hamiltonian operates directly on the vector $|j\rangle$ while the time-derivative operates on the complex exponential. For example, consider the 3p state of hydrogen:

$$\begin{aligned} i\hbar\frac{d}{dt}|\varphi_{3p}\rangle &= \widehat{H}_0|\varphi_{3p}\rangle \\ |3p\rangle\left(i\hbar\frac{d}{dt}e^{-i\omega_{3p}t}\right) &= e^{-i\omega_{3p}t}\left(\widehat{H}_0|3p\rangle\right) \\ |3p\rangle\left(\hbar\omega_{3p}e^{-i\omega_{3p}t}\right) &= e^{-i\omega_{3p}t}\left(\hbar\omega_{3p}|3p\rangle\right) \\ \hbar\omega_{3p}|\varphi_{3p}\rangle &= \hbar\omega_{3p}|\varphi_{3p}\rangle \end{aligned} \tag{4.3}$$

---

*Portions of "Section 4. Theory of Laser-Matter Interaction" have been reproduced from Hart, N. A. *Intensity-Resolved Above Threshold Ionization Yields of Atoms with Ultrashort Laser Pulses* Masters thesis, Texas A&M University, (2011). Copyright 2011 Nathan Andrew Hart

There is nothing special about the 3p state, as any state will satisfy an analogous equation. Moreover, there is nothing unique, in this sense, about the hydrogen atom, for the 3p eigenvector of sodium will obey the exact same properties for its own Hamiltonian. Note also that we do not assume to know the form of the eigenvector $|x\rangle\langle x|j\rangle$ or its Hamiltonian $\widehat{H}_0$. In this notation, the only things that separate one atom from another are the quantities of observables. This is useful theoretically since any physical quantities that we derive will be completely general to all atomic species. Let's consider a two level atom with a 3s ground state and a 3p excited state separated by an energy $\hbar\Delta\omega = \hbar(\omega_{3p} - \omega_{3s})$. The wavefunction for this system can be represented by a linear superposition of atomic eigenstates

$$|\psi\rangle = s_3(t)|3s\rangle e^{-i\omega_{3s}t} + p_3(t)|3p\rangle e^{-i\omega_{3p}t} \tag{4.4}$$

where $s_3(t)$ and $p_3(t)$ have been introduced as the complex probability amplitudes for the S and P states. For ease of notation we will drop the explicit time-dependence from the amplitudes by using the following definitions: $s_3 \equiv s_3(t)$ and $p_3 \equiv p_3(t)$. The wavefunction $|\psi\rangle$ is normalized such that

$$\begin{aligned} \langle\psi|\psi\rangle &= |s_3|^2 + |p_3|^2 \\ &= 1. \end{aligned} \tag{4.5}$$

Therefore, $\rho_{3s} = s_3^\dagger s_3$ and $\rho_{3p} = p_3^\dagger p_3$ represent the probabilities that the electron will occupy the 3s and 3p states respectively. This definition of the wavefunction $|\psi\rangle$ is known as the "interaction picture" since the amplitudes s_3 and p_3 only depend on the interaction Hamiltonian V_I.

We now want to know *how* the amplitudes s_3 and p_3 depend on the laser induced interaction. In the dipole approximation, the laser's electric field produces an effective potential energy of the electron as a function of the electric field and the spatial distance of the electron with respect to the nucleus:

$$\hat{V}_I = -e\boldsymbol{\mathcal{E}}(t) \cdot \hat{\boldsymbol{x}}. \tag{4.6}$$

Both the time dependent electric field $\boldsymbol{\mathcal{E}}(t) = (\mathcal{E}_1(t), \mathcal{E}_2(t), \mathcal{E}_3(t))$ and the spatial operator $\hat{\boldsymbol{x}} = (\hat{x}_1, \hat{x}_2, \hat{x}_3)^T$ are three dimensional vectors, and $-e$ is the charge of the electron. To simplify our discussion we will only consider the case for a linearly polarized electric field $\boldsymbol{\mathcal{E}}(t) = (\mathcal{E}_1(t),0,0)$. The time-dependent Schrodinger equation is then:

$$i\hbar \frac{d}{dt} = \hat{H}_0 + \hat{V}_I. \tag{4.7}$$

If we note that

$$\begin{aligned} \langle \varphi_{3s} | i\hbar \frac{d}{dt} | \psi \rangle = \langle \varphi_{3s} | \big(& i\hbar \big(\dot{s}_3 - i\omega_{3p} s_3 \big) | \varphi_{3s} \rangle \\ & + i\hbar \big(\dot{p}_3 - i\omega_{3p} p_3 \big) | \varphi_{3p} \rangle \big) \\ & = i\hbar \dot{s}_3 + \hbar \omega_{3p} s_3 \end{aligned} \tag{4.8}$$

then the equations of motion for the eigenstate amplitudes are

$$i\dot{s}_3 = -\frac{\mu_{3s,3p}\mathcal{E}_0}{2\hbar} \big(e^{-i(\omega_{3p,3s} - \nu)t} + e^{i(\omega_{3p,3s} + \nu)t} \big) p_3 \tag{4.9}$$

$$i\dot{p}_3 = -\frac{\mu_{3p,3s}\mathcal{E}_0}{2\hbar} \big(e^{i(\omega_{3p,3s} - \nu)t} + e^{-i(\omega_{3p,3s} + \nu)t} \big) s_3. \tag{4.10}$$

Here, the transition energy $\omega_{ij} = \omega_i - \omega_j$ and the dipole matrix element $\mu_{ij} = e\langle i | x_1 | j \rangle$. The linear polarization of the field implies that the dipole elements will be real valued. The two exponential terms $e^{i(\omega_{3p,3s} - \nu)t}$ and $e^{i(\omega_{3p,3s} + \nu)t}$ can be represented as vectors

rotating with time in the complex plane with the latter rotation faster than the former. If the laser is exactly on resonance with the ($3s \rightarrow 3p$) transition ($\nu = \omega_{3p,3s}$) then the first term averages to unity over one laser cycle while the second averages to zero. For this reason, when there is a near resonant transition, it is common to use the "rotating wave approximation" (RWA) where the second terms are set to zero ($e^{-i(\omega_{3p,3s}+\nu)t}$ and $e^{i(\omega_{3p,3s}+\nu)t} \rightarrow 0$). We can decouple equations 4.9 and 4.10 in the RWA using their derivatives $\ddot{s}_3$ and $\ddot{p}_3$ to get:

$$\ddot{s}_3 - i(\omega_{3p,3s} - \nu)\dot{s}_3 + \left(\frac{\Omega}{2}\right)^2 s_3 = 0 \tag{4.11}$$

$$\ddot{p}_3 - i(\omega_{3p,3s} - \nu)\dot{p}_3 + \left(\frac{\Omega}{2}\right)^2 p_3 = 0. \tag{4.12}$$

In Eq. 4.11 and 4.12,

$$\Omega = \frac{\mu_{3p,3s}\mathcal{E}_0}{\hbar}. \tag{4.13}$$

Using *Exp*(*iβt*) as a trial function with β being some constant, we see that the general solutions to these equations are:

$$s_3 = e^{-i(\omega_{3p,3s}-\nu)t/2}\left(Ae^{-i\Omega_R t} + Be^{i\Omega_R t}\right) \tag{4.14}$$

$$p_3 = e^{i(\omega_{3p,3s}-\nu)t/2}\left(Ce^{-i\Omega_R t} + De^{i\Omega_R t}\right). \tag{4.15}$$

The constants A, B, C and D can be solved for by setting problem-specific initial conditions on the amplitudes s_3 and p_3. Equations 4.14 and 4.15 imply that the electron population oscillates between the 3*s* and 3*p* states in a sinusoidal fashion. This is called "Rabi oscillation" or "Rabi flopping". And for a detuning $\delta/\hbar = (\omega_{3p,3s} - \nu)$, the Radi oscillation frequency is $\Omega_R = \sqrt{\Omega^2 + (\delta/4\hbar)^2}$.

4.2 Ponderomotive Energy

A free (continuum) electron in an oscillating electric field, $\boldsymbol{\mathcal{E}}(t) = \mathcal{E}_0\, Sin(\nu t)\, \hat{\boldsymbol{e}}_1$, absorbs kinetic energy and oscillates slightly out of phase with the field. The free electron however retains the frequency of the oscillating field since this field is the only applied force. This can be seen by defining the Lagrangian for linearly polarized continuous wave radiation:

$$L = \frac{1}{2} m_e \dot{\boldsymbol{x}}^2 - e\boldsymbol{\mathcal{E}} \cdot \boldsymbol{x} \tag{4.16}$$

Plugging equation (4.16) into Lagrange's equation of motion and integrating successively with respect to time gives the velocity and position of the "classical" electron:

$$x(t) = \frac{e\mathcal{E}_0}{\nu^2 m_e} Sin(\nu t) + \mathrm{v}_d t + x_0 \tag{4.17}$$

$$\dot{x}(t) = \frac{e\mathcal{E}_0}{\nu m_e} Cos(\nu t) + \mathrm{v}_d \tag{4.18}$$

where v_d is the drift velocity and x_0 is the initial position of the electron when it was ionized. Using the definitions $I_0 \equiv c\epsilon_0 \mathcal{E}_0^2/2$ and $\nu = 2\pi c/\lambda$ and neglecting the drift velocity, the time averaged kinetic energy or ponderomotive energy in electron volts (eV) of such an electron is:

$$U_P = \frac{1}{2} m_e \langle \dot{x}^2 \rangle \tag{4.19}$$

$$= \frac{e^2 \mathcal{E}_0^2}{4 m_e \nu^2} \tag{4.20}$$

$$= 9.33 \times 10^{-14} I_0[\mathrm{W/cm^2}] \lambda^2[\mu\mathrm{m^2}] \tag{4.21}$$

This quantity is important because an electron in a finite laser beam of sufficiently long pulse duration will on average gain this energy, $\widetilde{U}_P$, in the form of translational kinetic energy. Since for a Gaussian beam the local electric field amplitude as a function of the radius in cylindrical coordinates is:

$$\mathcal{E}(r, z = 0) = \mathcal{E}_0 \, e^{-r^2/w_0^2} \tag{4.22}$$

replacing $\mathcal{E}_0$ with $\mathcal{E}(r, 0)$ gives the local ponderomotive energy:

$$\widetilde{U}_P(r) = U_P e^{-2r^2/w_0^2} \tag{4.23}$$

where the azimuthal dependence has been neglected. This ponderomotive energy acts as an electric potential and provides a radial force $\boldsymbol{R}_P(r)$ to the electron due to the spatial variation in the field (see Figure 5).

$$\boldsymbol{R}_P(r) = -\boldsymbol{\nabla}_{\boldsymbol{r}} \widetilde{U}_P(r) \tag{4.24}$$

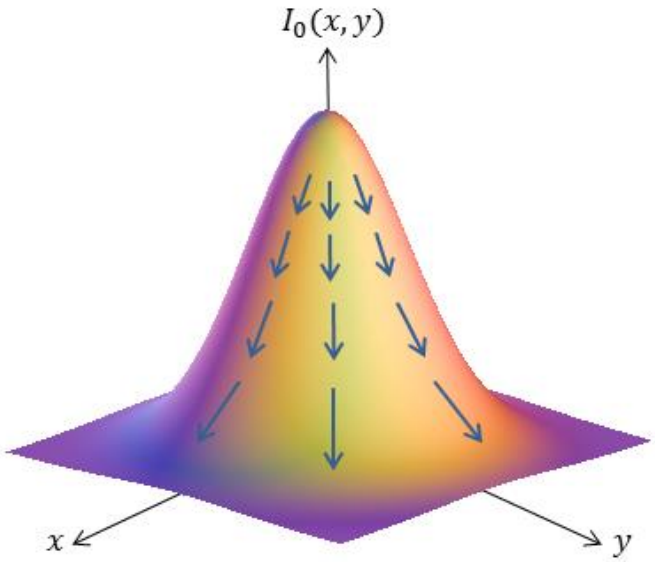

Figure 5. Electrons being pushed away from the center of the focus.

If the electron is initially at a radius r_0 prior to being accelerated, then the work done on the electron as it is pushed out of the field is:

$$W_P = -\int_{r_0}^{\infty} \boldsymbol{R}_P(r) \cdot d\boldsymbol{r} \tag{4.25}$$

$$= \widetilde{U}_P(r_0) \tag{4.26}$$

This means that the electron will gain a translational kinetic energy equal to the ponderomotive energy where it initially experienced the field. In calculating W_P, the upper bound of the integral implies that the radiation is continuous wave (CW). However, for sufficiently short pulses the electron may not have enough time to be displaced out of the field and, as a result, not gain the full $\widetilde{U}_P(r_0)$. A rough estimate of the necessary laser parameters for equation (4.26) to hold can be obtained by equating the kinetic energy of the free electron to $U_P/2$ and finding the distance it travels for pulse duration τ_d. For example, a pulse of wavelength λ = 800 nm, duration τ_d = 100 fs and peak intensity $I_0 = 10^{13}$ W/cm^2 would move an electron less than 50 nm away from the center of the beam. This is negligible compared to a typical beam waist of $w_0 \sim 10$ μm, and as a result the upper bound of the integral (4.25) is approximately r_0.

When an electric field is applied to an atom, the energy levels change by a value known as the Stark shift. Through a lengthy quantum mechanical calculation[27] it is found that the dynamic or AC Stark shift of an atomic energy level $E_i \ll \hbar\omega$ due to an oscillator field is approximated by:

$$\delta E_i \approx \frac{e^2 \mathcal{E}(r_0)^2}{4 m_e \nu^2} \tag{4.27}$$

$$= U_P(r_0) \tag{4.28}$$

It is remarkable that the AC Stark shift under the above restriction is equal to the ponderomotive energy $U_P(r_0)$ provided by the field. One consequence of this is that the highest "continuum" state $E_i \approx 0$, is increased in the following manner: $E_i \rightarrow E_i + \delta E_i$. To be ionized the electron must now gain an energy:

$$E > U_P(r_0) + V_{IE} \tag{4.29}$$

where V_{IE} is the ionization energy of the unperturbed atom (see Figure 6).

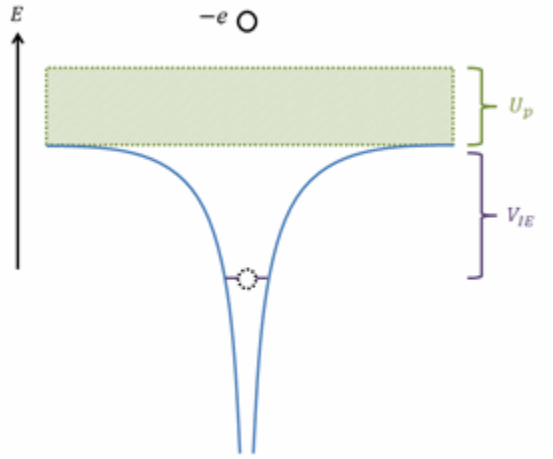

Figure 6. Ionization in a low intensity field.

Once ionized the electron is pushed along the radiation energy gradient towards lower ponderomotive energies. For sufficiently long laser pulse durations ($\tau_d \gg 1$ ps) and large intensities ($I_0 > 10^{13}$ W/cm^2) at λ = 800 nm the electron will regain the kinetic energy $U_P(r_0)$ lost through the AC Stark shift as it travels away from the atom. However, for short laser pulses ($\tau_d < 50$ fs) even intensities as high as $I_0 \sim 10^{13}$ W/cm^2 will not be sufficient to recover the lost energy.

4.3 The AC Stark Shift

It is relevant to introduce two ways in which the probability amplitude is commonly defined. For the "Schrodinger picture", the time derivative of the eigenfunction yields the atomic energy of the eigenstate. However, in the "Interaction picture", the time derivative yields the Rabi frequency. The wave functions are expressed as:

Schrodinger picture

$$|\psi\rangle = \sum_{j=1}^{\infty} S_j|js\rangle + \sum_{k=1}^{\infty} P_k|kp\rangle + \sum_{l=1}^{\infty} D_l|ld\rangle + \cdots \tag{4.30}$$

Interaction picture

$$|\psi\rangle = \sum_{j=1}^{\infty} s_j|js\rangle e^{-i\omega_j t} + \sum_{k=1}^{\infty} p_k|kp\rangle\, e^{-i\omega_k t} + \sum_{l=1}^{\infty} d_l|ld\rangle e^{-i\omega_l t} + \cdots \tag{4.31}$$

where $|js\rangle$, $|kp\rangle$ and $|ld\rangle$ are the Eigen kets for the *S*, *P* and *D* atomic states and *j*, *k* and *l* are the principle quantum numbers. For example, $|3d\rangle$ is the Eigen ket for the 3*d* atomic state with principle quantum number 3 and azimuthal quantum number 2. This notation is used here for convenience and clarity. Other text discussing the density matrix or amplitude methods of solving the Schrodinger equation use a different notation. Similarly, ω_j, ω_k and ω_l are the eigenfrequencies such that ω_j would be the eigenfrequency for the *js* atomic state ($\omega_k \equiv \omega_{kp}$ and $\omega_l \equiv \omega_{ld}$). The atomic amplitudes are defined as

$$S_j \equiv s_j e^{-i\omega_j t} \tag{4.32}$$

$$P_k \equiv p_k e^{-i\omega_k t} \tag{4.33}$$

$$D_l \equiv d_l e^{-i\omega_l t}\,. \tag{4.34}$$

Note that, the amplitudes P_1, D_1 and D_2 are identically zero since the $1p$, $1d$ and $2d$ states do not exist. In principle, the wave functions 4.30 and 4.31 also have F, G, H, I, K, … azimuthal states as well. For simplicity, we shall limit the azimuthal quantum number to be less than 3. We can find the equations of motion for the amplitudes by solving the Schrodinger. For example, the rate equation for s_j can be found by

$$\left\langle js\left| i\hbar \frac{d}{dt} \right|\psi\right\rangle = \langle js|H_0 + V_I|\psi\rangle. \tag{4.35}$$

The rate equations in the Interaction picture are therefore

$$i\hbar \dot{s}_j = -\sum_{k=2}^{\infty} \mu_{jk}\mathcal{E}_0 Cos(\nu t) e^{i\omega_{jk}t} p_k \tag{4.36}$$

$$i\hbar \dot{p}_k = -\sum_{j=1}^{\infty} \mu_{kj}\mathcal{E}_0 Cos(\nu t) e^{i\omega_{kj}t} s_j - \sum_{l=3}^{\infty} \mu_{kl}\mathcal{E}_0 Cos(\nu t) e^{i\omega_{kl}t} d_l \tag{4.37}$$

$$i\hbar \dot{d}_l = -\sum_{k=2}^{\infty} \mu_{lk}\mathcal{E}_0 Cos(\nu t) e^{i\omega_{lk}t} p_k - \sum_{m=4}^{\infty} \mu_{lm}\mathcal{E}_0 Cos(\nu t) e^{i\omega_{lm}t} f_m. \tag{4.38}$$

where $\omega_{jk} = \omega_j - \omega_k$, $\omega_{kl} = \omega_k - \omega_l$ and so on. To derive the AC Stark shift for a given S state, we first integrate Eq. 4.37 to obtain p_k and plug it into Eq. 4.36. Dividing by $i\hbar$ and showing only the s_j terms, we get

$$\dot{s}_j = -\sum_{k=2}^{\infty} \left(\frac{\mu_{jk}\mathcal{E}_0}{\hbar}\right) Cos(\nu t) e^{i\omega_{jk}t} \left(\left(\frac{\mu_{kj}\mathcal{E}_0}{\hbar}\right) \int_{-\infty}^{t} Cos(\nu t') e^{i\omega_{kj}t'} s_j dt' \right) + \cdots \tag{4.39}$$

$$= \left(\frac{i}{2} \sum_{k=2}^{\infty} \left| \frac{\mu_{jk} \mathcal{E}_0}{\hbar} \right|^2 Cos(\nu t) e^{i\omega_{jk} t} \left(\frac{e^{i(\omega_{kj}+\nu)t}}{\omega_{kj}+\nu} + \frac{e^{i(\omega_{kj}-\nu)t}}{\omega_{kj}-\nu} \right) \right) s_j + \cdots \tag{4.40}$$

$$= i \left(\sum_{k=2}^{\infty} \left| \frac{\mu_{jk} \mathcal{E}_0}{2\hbar} \right|^2 \left[\left(\frac{1}{\omega_{kj}+\nu} + \frac{1}{\omega_{kj}-\nu} \right) + \left(\frac{e^{i2\nu t}}{\omega_{kj}+\nu} + \frac{e^{-i2\nu t}}{\omega_{kj}-\nu} \right) \right] \right) s_j + \cdots \tag{4.41}$$

where the slow varying approximation has been used for s_j. The term in the brackets [ ] of Eq. 4.41 represents the time dependent energy of the atomic state *S* accurate to second order in the electric field $\mathcal{E}_0$. If we use the rotating wave approximation (RWA) for Eq. 4.41, we see that the terms containing *Exp*(*ivt*) and *Exp*(-*ivt*) average to zero and we obtain the second order energy correction (AC Stark shift)

$$E_j^{(2)} \approx \sum_{k=2}^{\infty} \left| \frac{\mu_{jk} \mathcal{E}_0}{2\hbar} \right|^2 \left(\frac{1}{\omega_{kj}+\nu} + \frac{1}{\omega_{kj}-\nu} \right) \tag{4.42}$$

$$= \sum_{k=2}^{\infty} \left| \frac{\mu_{jk} \mathcal{E}_0}{2\hbar} \right|^2 \left(\frac{\omega_{kj}}{\omega_{kj}^2 - \nu^2} \right). \tag{4.43}$$

The infinite sum cannot be calculated exactly. However, it is known that the second order correction to atomic Rydberg state energies due to the continuum states is equal to the average kinetic energy of an electron in the continuum Eq. 4.20. Therefore, a computationally practical expression for the AC Stark shift is

$$E_j^{(2)} = \frac{e^2 \mathcal{E}_0^2}{4 m_e \nu^2} + \sum_{k=2}^{N_p} \left| \frac{\mu_{jk} \mathcal{E}_0}{2\hbar} \right|^2 \left(\frac{\omega_{kj}}{\omega_{kj}^2 - \nu^2} \right) \tag{4.44}$$

$$= U_p + \sum_{k=2}^{N_p} \left|\frac{\mu_{jk}\mathcal{E}_0}{2\hbar}\right|^2 \left(\frac{\omega_{kj}}{\omega_{kj}^2 - \nu^2}\right).$$

where N_p is the number of "relevant" bound *P* states. Similarly, for the *P* states

$$E_k^{(2)} = U_p + \sum_{j=1}^{N_s} \left|\frac{\mu_{kj}\mathcal{E}_0}{2\hbar}\right|^2 \left(\frac{\omega_{jk}}{\omega_{jk}^2 - \nu^2}\right) + \sum_{l=1}^{N_d} \left|\frac{\mu_{kl}\mathcal{E}_0}{2\hbar}\right|^2 \left(\frac{\omega_{lk}}{\omega_{lk}^2 - \nu^2}\right). \quad (4.45)$$

4.4 Multiphoton Ionization

There are three general ways in which photoionization can be described. For the lowest intensities, a process analogous to the photoelectric effect occurs. In the photoelectric effect, an atom is ionized when a bound electron absorbs a photon whose energy $\hbar\nu$ exceeds the atomic potential energy V_{IE}. The photoelectric effect follows the rule of being independent of the radiation intensity because the decay rate of the excited atom is much faster than the absorption rate of new photons. Thus, for a wide range of intensities (in noble gasses like xenon: $I_0 < 10^{11}$ W/cm^2), photons with energy $\hbar\omega \ll V_{IE}$ are reemitted by the atom (see Figure 7).

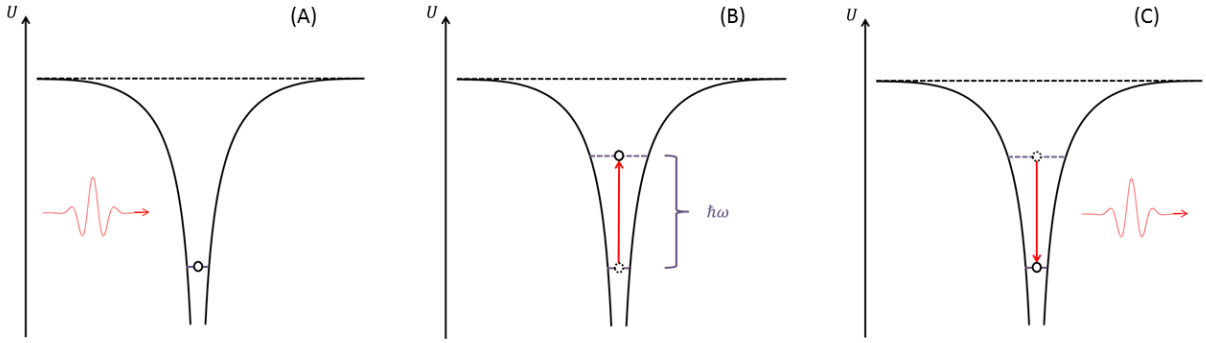

Figure 7. Photon absorption and spontaneous reemission. The photon in red and the unexcited atom (A). The excited atom (B). Spontaneous emission of a photon (C).

However, increasing the radiation intensity I_0 above a certain threshold, called the appearance intensity I_{ap}, allows the photon absorption rate to exceed the decay rate. It is then possible to ionize the atom through an absorption of several photons as the sum of the photon energies exceeds the ionization potential.

$$\sum_i \hbar\nu_i > V_{IE} \tag{4.46}$$

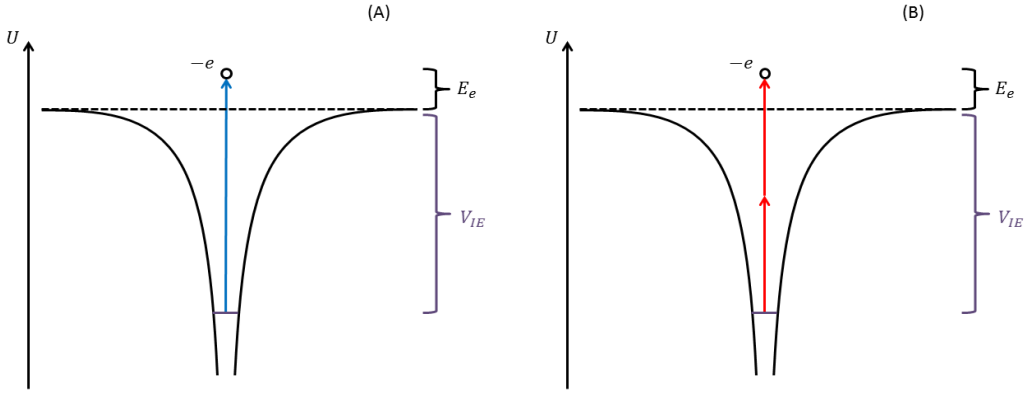

Figure 8. Photoionization due to the photoelectric effect (A) and two-photon absorption (B).

This process is referred to as multi-photon ionization (MPI), and can be viewed as a generalization of the photoelectric effect (see Figure 8). For a broadband laser the electron can absorb several photons each with a unique energy present in the spectrum. But for simplicity, equation (4.47) depicts the interaction of monochromatic radiation with the atom "*A*":

$$n\hbar\nu + A \rightarrow e^{-} + A^{+} \tag{4.47}$$

Where *n* is the number of photons absorbed, $\hbar\nu$ is the energy of each photon, e^{-} is the ejected electron, A is the prepared target, and A^{+} is the final state of the target. The energy of the electron is then:

$$KE = n\hbar\nu - V_{IE} \tag{4.48}$$

where V_{IE} is the potential energy of the electron for atom A. The radiation field is viewed as perturbation to the atomic potential well and perturbation theory can be used to find the ionization probability $P(I)$. $P(I)$ is proportional to the radiation intensity *I* to the power equal to the order of the multiphoton ionization:

$$P(I) \propto I^{n} \tag{4.49}$$

where *n* satisfies $1 \geq n - \frac{V_{IE}}{\hbar\omega} \geq 0$.

In general, the parameter

$$K \equiv \frac{Ln\big(P(I)\big)}{Ln(I)} \tag{4.50}$$

is use to characterize the absorption of radiation energy as function of intensity. *K* is a measure of the absorption process, independent of the absorption mechanism. For multiphoton ionization $K \approx n$. However, for resonant multiphoton excitation or tunneling

ionization, *K* maybe significantly greater or smaller than the number of photons required for that process.

4.5 Tunneling Ionization

As an atom interacts with an oscillating electric field, the Coulomb potential of the initially unperturbed atom begins to sway back and forth in phase with the field. This is related to the variations of the effective potential of the atom:

$$V(x) = -\frac{1}{4\pi\epsilon_0}\frac{e^2 Z}{x} - e\boldsymbol{\mathcal{E}}_0(t)\cdot\boldsymbol{x} \tag{4.51}$$

$$= -\frac{1}{4\pi\epsilon_0}\frac{e^2 Z}{x} - e(\boldsymbol{\mathcal{E}}_0\,\mathrm{Sin}(vt))\cdot\boldsymbol{x} \tag{4.52}$$

where *Z* is the charge state of the atom, $\boldsymbol{x}$ is the distance away from the nucleus, $\mathcal{E}_0$ is the radiation field amplitude, *v* is the frequency of the oscillation and t is the time variable. For sufficiently large electric fields, this effective potential of the atom will "dip" down, creating a well that the bound electron can tunnel out of (see Figure 9). This is referred to as tunneling ionization (TI).

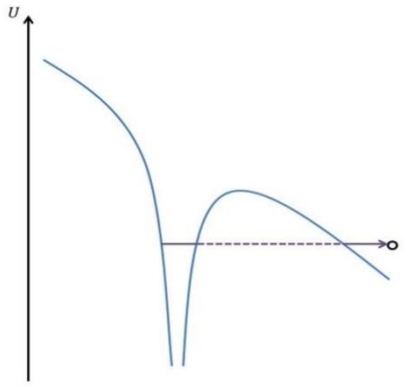

Figure 9. Tunneling Ionization. The electron tunnels (dashed line) out of the atom and into the continuum.

The average tunneling time τ is determined by the potential barrier height and thickness. The Keldysh tunneling parameter γ is a metric for determining when the intensity is high enough to describe the ionization mainly through a tunneling process. The parameter γ has two equivalent representations[28]:

$$\gamma = \frac{\nu\tau}{2\pi} \tag{4.53}$$

$$= \left(\frac{V_{IE}}{2U_P}\right)^{\frac{1}{2}} \tag{4.54}$$

where ω is the frequency of the oscillating electric field, V_{IE} is the ionization potential and U_P is the ponderomotive potential. The first representation gives an intuitive picture of the tunneling process. If the period of the laser, $2\pi/\nu$, is comparable to the tunneling time, τ, then tunneling becomes probable. Hence $\gamma \simeq 1$ is a necessary but not sufficient condition to imply electron tunneling out of the atom. The second representation is more useful for experimental research because it can be easily calculated. V_{IE} is usually found in published atomic and molecular reference materials and U_P can be calculated from equation (4.21). The utility of the Keldysh parameter itself comes from its ability to distinguish between MPI ($\gamma \gg 1$) and TI ($\gamma \simeq 1$). However, when γ approaches unity a mixture of the two processes maybe seen in experiment because both MPI and TI become probable to occur.

4.6 Over the Barrier Ionization

If the laser intensity is large enough, the Coulomb potential may no longer be higher than the unperturbed ground state. In this case, there is no longer a bound state for the

outer most electron. This electron is then said to be freed through Over The Barrier Ionization (OTBI).

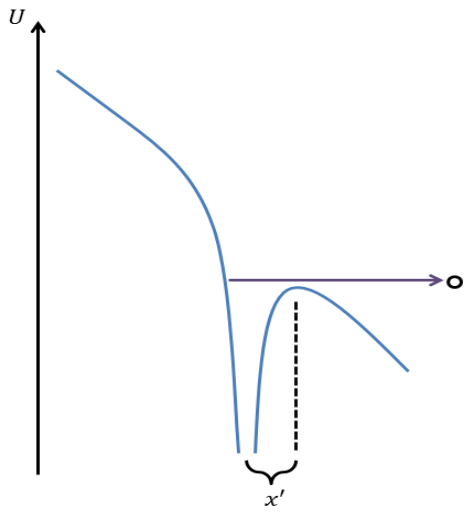

Figure 10. A graphical depiction of over the barrier ionization. The right potential barrier becomes lower than the ground state at the energy of the purple arrow.

To gain a qualitative understanding of the process we ignore any longitudinal electric field components of the uncollimated beam and reduce equation (4.51) to one dimension. This paraxial approximation is only valid where the beam makes a negligible angle with the axis of propagation. The minimum electric field required to induce OTBI can then be found by first noting that the condition for OTBI is the following:

$$-V_{IE} > -\frac{1}{4\pi\epsilon_0}\frac{e^2 Z}{|x'|} - e\mathcal{E}_0 x' \tag{4.55}$$

This means that the ground state energy of the unperturbed atom is greater than the peak potential energy of the atom in the radiation field (see Figure 10). We can find x' from the equation $dV(x = x')/dx = 0$. This gives:

$$x' = \sqrt{eZ/4\pi\epsilon_0\mathcal{E}_0} \tag{4.56}$$

for the distance away from the nucleus where the potential starts to dip back down. Plugging equation (4.56) into equation (4.55) gives:

$$\mathcal{E}_0 > \frac{\pi\epsilon_0 {V_{IE}}^2}{e^3 Z} \tag{4.57}$$

$$I_0 > c\epsilon_0^3 \frac{\pi^2 {V_{IE}}^4}{2\, e^6 Z^2} \tag{4.58}$$

Note that while MPI and TI are functions of two laser parameters I_0 and λ, OTBI is only a function of I_0. This is because of the relatively small mass, and thus inertia, of the electron. An unbound electron with one unit of photon energy $\hbar\nu$ < 5 eV will, in half a laser cycle, travel a distance more than 10 times the Bohr radius a_0. For comparison the neutral xenon atom is approximately twice the Bohr radius. This means that for a wide range of photon energies the wavelength dependence is negligible.

4.7 Above Threshold Ionization

During irradiation, electrons in the target atom or molecule may absorb more photons than are needed to exceed the ionization threshold V_{IE}. The absorption of additional photon energy above the minimum ionization threshold is referred to as Above Threshold Ionization (ATI) (see Figure 11). This is expressed mathematically by:

$$E_e > \hbar\nu \tag{4.59}$$

where E_e is the kinetic energy of the electron in the continuum due to photon absorption. ATI may, and typically does occur in all three of the above mentioned ionization mechanisms (MPI, TI and OTBI).

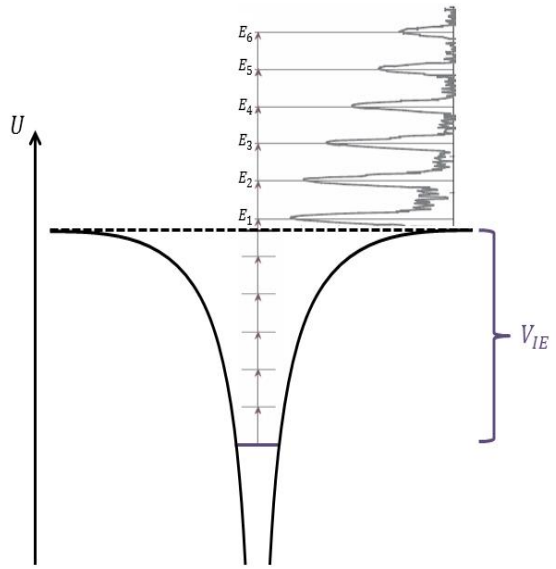

Figure 11. A graphical depiction of the ATI process. Here the electron absorbs an integer number of photons whose total energy exceeds $\boldsymbol{V_{IE}}$ by more than one photon. The figure shows the graph of a numerical simulation from Paulus, Nicklich, Zacher, Lambropoulos, & Walther (1996) superimposed onto a drawing of an atomic potential well.

If the intensity of the radiation is large, such that the energy of the electron is:

$$E = n\hbar\nu - (V_{IE} + U_P) \tag{4.60}$$

$$< 0 \tag{4.61}$$

the electron will not escape the atom and thus will not appear in the ATI spectrum. As intensity increases, the ponderomotive shift of the continuum may exceed the energy of the lower energy peaks successively (see Figure 12). In such a case, channel closing is said to have occurred and the respective peaks appear suppressed.

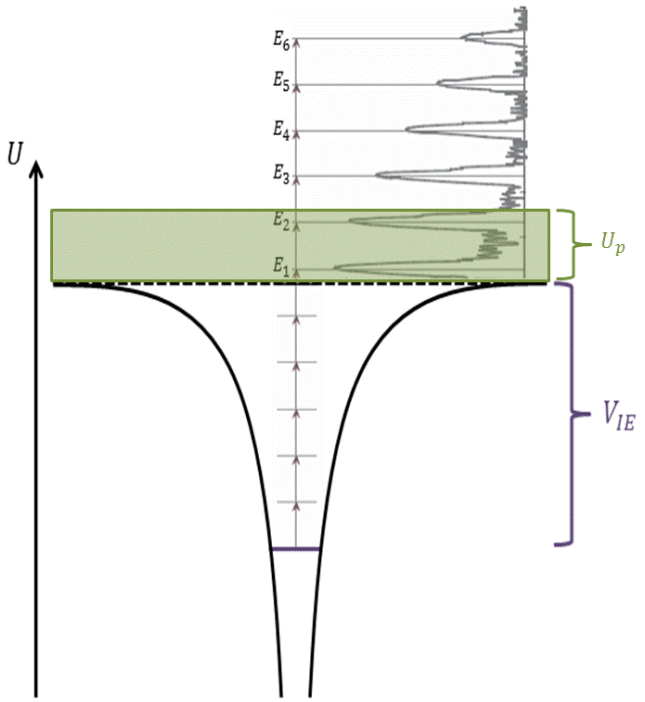

Figure 12. Channel closing for the $\boldsymbol{E_1}$ and $\boldsymbol{E_2}$ peaks of a simulated ATI spectrum.

For sufficiently short pulses low energy electrons will still appear in the ATI spectrum due to a red-shifting of the entire spectrum when the electron does not have enough time in the field to regain the ponderomotive energy.

4.8 Freeman Resonance

AC Stark shifts can also lead to REMPI when an intermediate (dipole-allowed) energy level shifts into an integer photon resonance. This typically occurs for laser pulses that have an integer photon resonance blue-detuned from an intermediate resonance by an amount that is greater than half the bandwidth. As the intensity rises on the front of the pulse, a field-induced AC Stark shift causes the Lorentzian density-of-

states distribution for the intermediate level to overlap with the bandwidth of the laser. Since this overlap satisfies the resonance condition, electron population of the shifted intermediate state is enhanced. This dynamic resonance is referred to as a Freeman resonance which was first spectrally resolved by Freeman *et. al.*[1] in the electron energy spectrum.

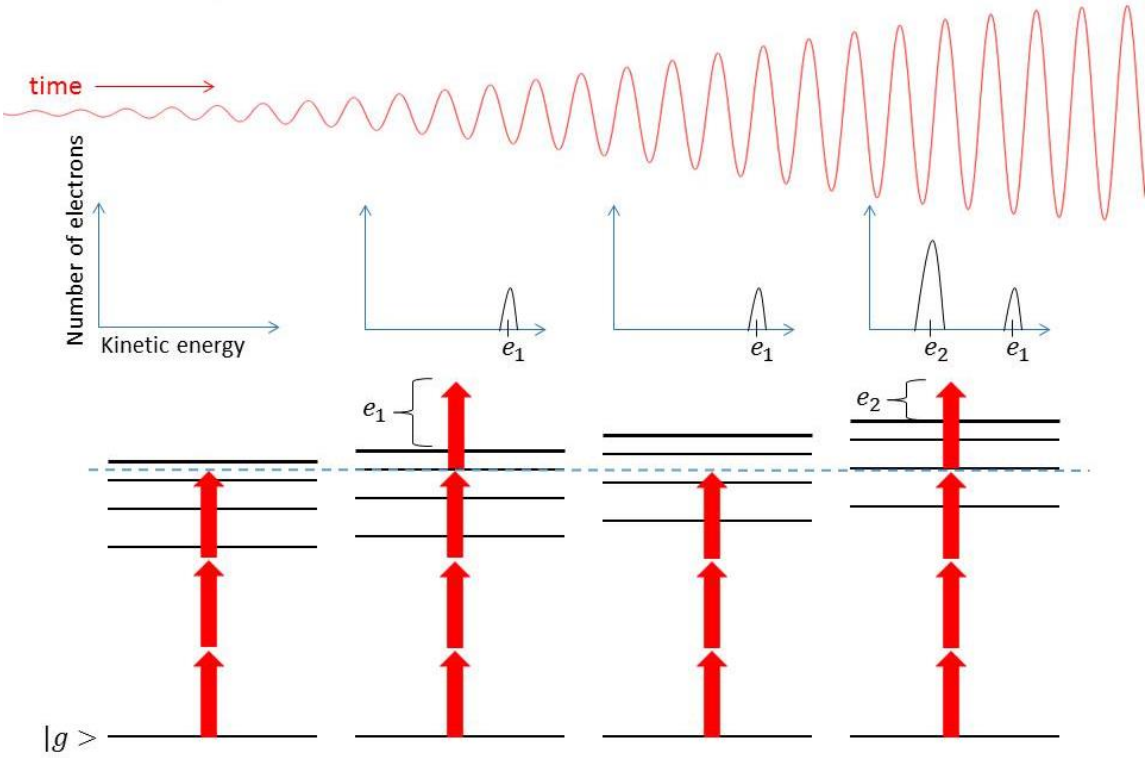

Figure 13. A schematic depiction of the how Freeman resonances influence ionization. A portion of the laser pulse is depicted at the top. As the time dependent intensity rises, the Rydberg states Stark shift relative to the ground state and scan across the three photon resonance.

Freeman resonances are typically associated Rydberg states because bound states closest to the continuum have the largest AC Stark shifts, and lower bound states can undergo a large Rabi splitting which complicate the Freeman resonance interpretation. For this same reason Freeman resonances are commonly associated with ionization. The

high intensities required to create these multiphoton resonances close to the ionization potential are typically sufficient to promote the electron from a Rydberg state to the continuum by the addition of at least one photon in energy. Ionization is then measured from the dynamically resonant Rydberg state, and the electrons excess kinetic energy propels it out of the laser focus (see subsection 4.4 Multiphoton Ionization). If *T*, the time it takes for the electron to exit the focus, is much greater than the pulse duration, $T \gg \tau_p$, then the electron will not regain the ponderomotive energy lost from the upward shift of the continuum (see section 4.2 Ponderomotive Energy) and the energy of the atomic Rydberg states can be resolved in the ATI spectrum[1]. The higher order ATI peaks will tend to show less spectroscopic information since those electron travel much faster away from the focus (smaller *T*) and will regain more of their ponderomotive energy back and lower order (slower) ATI electrons.

4.9 Frequency Generation

One important thing to keep in mind is that when the electron accelerates relative to the ion core of the atom, radiation is generated which is proportional to the time-dependent polarization. Moreover, the time-dependent polarization is related to atomic transitions that occur during the acceleration. Since coherent radiation is capable of polarizing atoms, the laser interaction produces an output spectrum which is characteristic of the atomic potential. The acceleration of the electron relative to the ion core is characterized by the dipole acceleration (see section 4.3 for notation)

$$a(t) = \frac{d^2}{dt^2}\langle\psi|\hat{\mathbf{x}}|\psi\rangle \tag{4.62}$$

$$= \frac{1}{e}\frac{d^2}{dt^2}\left[\sum_{j,k=1}^{\infty} \mu_{jk} s_j^* p_k \mathrm{e}^{i\omega_{jk}t} + \sum_{k,l=1}^{\infty} \mu_{kl} p_k^* d_l \mathrm{e}^{i\omega_{kl}t} + \cdots + c.c.\right]$$

$$= \frac{d^2}{dt^2} x(t)$$

The output optical spectrum is proportional to the square magnitude of the acceleration spectrum. To find the spectrum of the acceleration we take its Fourier transform

$$\begin{aligned} a(\omega) &= \frac{1}{\sqrt{2\pi}} \int_{-\infty}^{\infty} a(t) \mathrm{e}^{-i\omega t} dt \\ &= \frac{1}{\sqrt{2\pi}} \int_{-\infty}^{\infty} \frac{d^2}{dt^2} x(t) \mathrm{e}^{-i\omega t} dt \end{aligned} \tag{4.63}$$

$$= \frac{-\omega^2}{\sqrt{2\pi}} \int_{-\infty}^{\infty} x(t) \mathrm{e}^{-i\omega t} dt. \tag{4.64}$$

Equation 4.64 comes from an integration by parts of Eq. 4.63 and assuming $x(-\infty) = x(\infty) = 0$. The output spectrum $W(\omega)$ from the laser-atom interaction in the forward direction is then given by[29]

$$\begin{aligned} W(\omega) &= \frac{e^2}{4\epsilon_0^2 c^2 \omega^2} |a(\omega)|^2 \\ &= \frac{e^2 \omega^2}{4\epsilon_0^2 c^2} |x(\omega)|^2. \end{aligned} \tag{4.65}$$

5. PROPERTIES OF SODIUM ATOMS AND VAPOR

The sodium is classified as an alkali metal atom with the atomic symbol Na and atomic number 11 (eleven protons). Its atomic mass is 22.99H, and its electron configuration is ($1s^2 2s^2 2p^6 3s^1$). $^{23}_{11}$Na is the only stable isotope with the second most stable isotope, $^{22}_{11}$Na, having a half-life of 2.6 years[30]. At room temperature and atmospheric pressure, sodium has a box centered cubic crystal structure with a metallic, silver-like appearance[31] (see Figure 14).

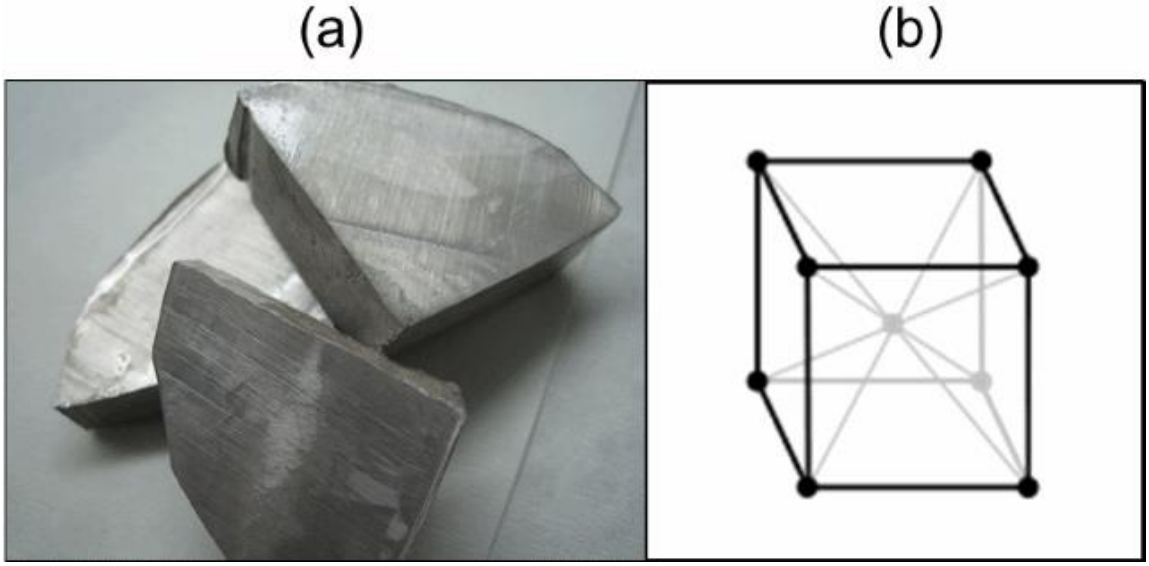

Figure 14. (a) a photograph of three blocks of metallic sodium. (b) the box centered cubic crystal structure of sodium. Each node represents a Na atom[32,33].

The melting point of pure sodium is 97.794 °C, and its vapor pressure P_v of may be calculated by the following empirical formulae[34]:

$$Log_{10}(P_v) = 133.429 - \frac{9302.868}{T} + 0.031144\,T - 49.3768\,Log_{10}(T) \tag{5.1}$$

in the solid phase and:

$$Log_{10}(P_v) = 10.8642 - \frac{5619.406}{T} + 0.00000345\,T - 1.04111\,Log_{10}(T) \tag{5.2}$$

in the liquid phase.

The energy level diagram for the sodium atom is pictured below in Figure 15. The states are ordered according to their angular momentum horizontally and their principal quantum number vertically.

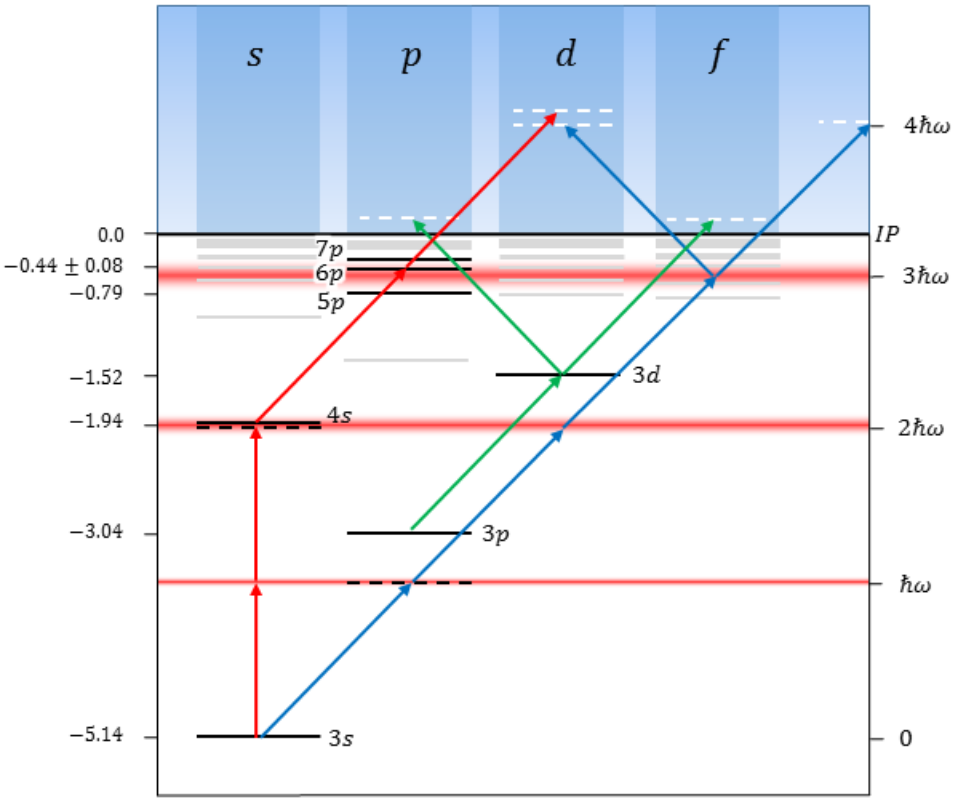

Figure 15. An energy level diagram of the sodium atom (Na). The left axis displays the energy of select atomic levels in units of [eV], while the right axis has units of the photon energy ($\hbar\nu$ = 1.55 eV). All arrows represent one photon energy. The different color arrows represent competing paths to the continuum with the red path being the most dominant.

Selected energy levels of sodium in units of electron volts are presented in Table 1[35].

Only the energy states considered in the scope of this research are listed.

Table 1. A table of the energies for the most active atomic states of Na in units of [eV]. The four columns s, p, d, f denote the angular momentum of each state, while the left most column displays the principal quantum number for each row. In the case of doublets states, the number in the table represents the larger value.

n	*s*	*p*	*d*	*f*
7		7p = -0.36		7f = -0.28
6		6p = -0.51		6f = -0.38
5	5s = -1.02	5p = -0.79		5f = -0.54
4	4s = -1.95	4p = -1.39		4f = -0.85
3	3s = -5.14 eV	3p = -3.04 eV	3d = -1.52 eV	

6. DESCRIPTION OF EXPERIMENTS IN SODIUM

We conducted three main types of experiments (Intensity Scan, Chirp Scan and Spectrum Scan), which are described in more detail below. For each measurement, a number of experimental parameters were recorded in an automated fashion. These parameters include the laser spectrum, average laser power and position of the grating compressor (SOD). The sodium oven temperature (vapor pressure) was also recorded, but was typically maintained at around 256 ℃.

For an Intensity Scan, we start by measuring an electron time-of-flight (TOF) spectrum at some average laser power. The TOF spectrum and all the recorded parameters of the experiment are saved as the data for that measurement. Then the laser power is increased while maintaining all other laser parameters (i.e. chirp and spectrum) constant. The data for this new measurement of a slight higher power is then saved. This process, of changing the power monotonically and saving the data, is repeated until some desired maximum power is reached. Since the laser pulse intensity is linearly proportional to the average power of the laser, the intensity for each data set can be calculated. In a typical IS, the intensity is scanned from 5×10^{11} - 6×10^{12} W/cm^2.

A Chirp Scan is analogous to the Intensity Scan in that it varies only one independent variable, the SOD, while keeping the laser power and spectrum for each measurement constant. To accomplish this, first an electron TOF measurement is taken at some initial SOD and the data (TOF spectrum and experimental parameters) is saved. The SOD is then decreased, and another electron TOF measurement is acquired and saved. The

process of decreasing the SOD and saving the data is iterated until some final desired chirp is attained. In a typical Chirp Scan, the SOD is varied from +3000 to -3000 fs^2.

In the Spectral Scan, the independent variable was the wavelength λ of laser radiation that was removed before the beam was focused into the sodium vapor. The desired intensity and chirp were determined prior to and kept constant throughout the scan. To be more specific, we started with the smallest wavelength λ of radiation that could be measured from our laser pulse and blocked radiation in the range of $\lambda \pm 2$ nm. Then, the data for an electron TOF was measured and saved. Subsequently, the value of λ was increased by approximately 2 nm such that roughly half of the new blocked region overlapped with the previous region, and another measurement cycle was commenced. This process was iterated over a spectral region ~40 nm wide (twice the bandwidth) and centered on 800 nm.

7. EXPERIMENTAL RESULTS

In Figure 16, Intensity Scans (IS) for three different values of the second order dispersion (SOD) are displayed on the left hand side while a single ATI energy spectrum for the corresponding SOD is displayed to its right. The location of the peaks on the energy axis was calibrated by comparing the data with known atomic state energies from the National Institute of Standards and Technology (NIST) (see section 5. Properties of Sodium Atoms and Vapor). In each set of spectra, one-photon ionization from the 5*p* (≈ 0.75 eV) and 6*p* (1.03 eV) energy levels provide the most prominent electron peaks. These peaks, along with all others below 1.55 eV, are shown in the data one photon ($\hbar\nu$ ≈ 1.55 eV) in energy away from their respective bound state (-0.79 eV for 5*p* and -0.44 eV for 6*p*) and comprise the threshold peak. Only the negative chirp IS shows significant ionization from 7*p*, which is shown to the right of the 6*p* peak at 1.19 eV.

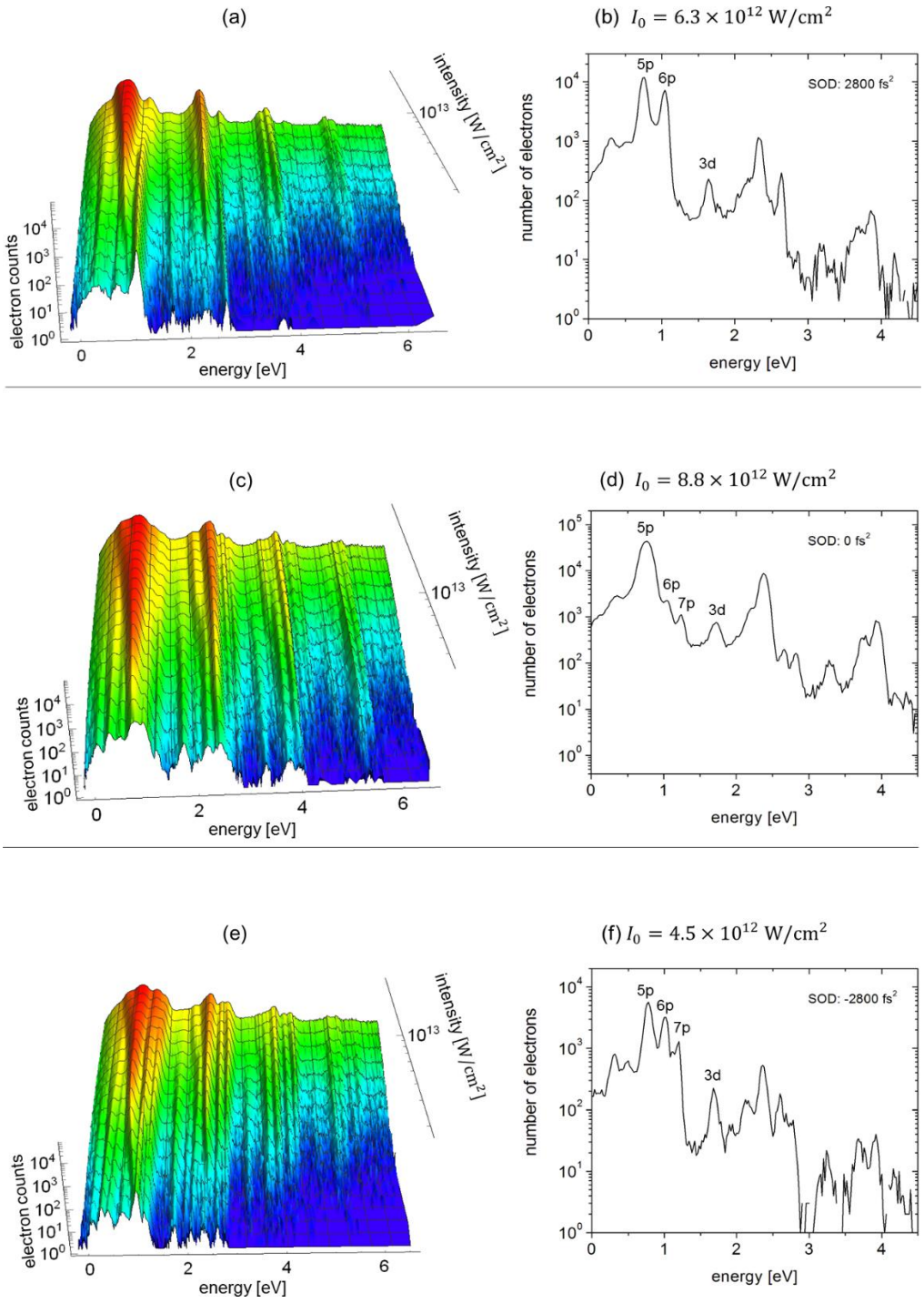

Figure 16. Experimental intensity scans for chirped pulses with SOD values of (a) 2800 fs^2, (c) 0 fs^2, and (e) -2800 fs^2. Corresponding photo-electron spectra are shown to their right for the specific intensities (b) 6.3×10^{12} W/cm^2, (d) 8.8×10^{12} W/cm^2 and (f) 4.5×10^{12} W/cm^2. The 5*p*, 6*p*, 7*p* and 3*d* states are labeled for points of reference. All spectra were measured at a Na vapor pressure of ~ 10^{-3} mbar.

No ponderomotive plateaus are present in the ATI spectrum because, at least two photon orders of the ATI spectrum are needed to define a plateau. At $I_0 = 2.5\times10^{12}$ W/cm^2, $2U_p$ is equal to 0.3 eV, which is less in energy than the center of the threshold peak (1 eV). $10U_p$ = 1.5 eV and is less than the energy of the first above threshold peak (2^{nd} photon order). Therefore, we expect each ATI peak to yield less electrons than the previous photon order.

At the lowest laser intensities, the sub-peak corresponding to direct ionization from the 3*s* ground state is degenerate in energy with 6*p*. This is because, in the unperturbed atom, 6*p* is in three-photon resonance with the ground state (3s→→→6p). However, as the intensity increases, the ionization potential also rises proportionally by an amount equal to the ponderomotive energy of the laser field U_p. This leaves less residual energy in the continuum for an ionization directly from the ground state, and the 3*s* peak shifts significantly to lower energies (Figure 17).

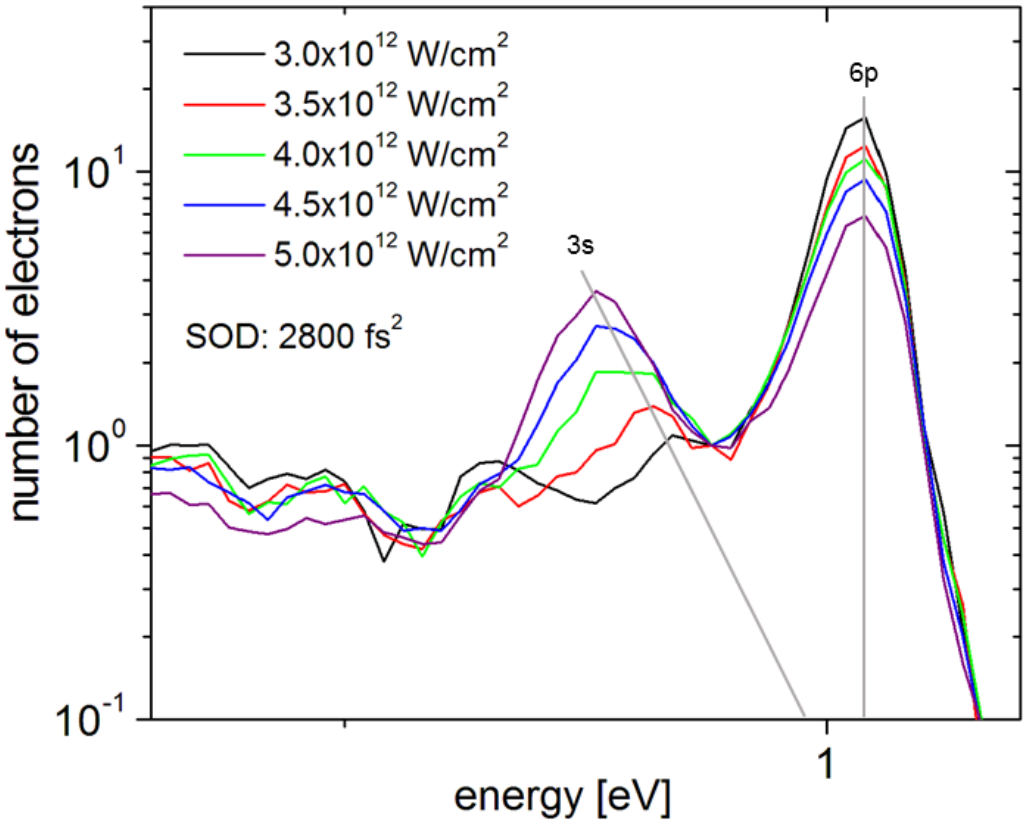

Figure 17. Experimental photo-electron spectrum for a positively chirped pulse showing the relative shift of the 3*s* ground state with respect to the continuum. The 6*p* Rydberg state is Stark shifted by an amount that is approximately equal to the ponderomotive shift of the continuum.

Ionization from the Rydberg levels is largely immune to this effect because these levels, like the continuum, incur a positive AC Stark shift $E^{(2)}$ that is roughly equal to U_p. As 5*p* Stark shifts into three-photon resonance (3*s*→→→5*p*), the 3*s* peak smoothly becomes the 5*p* peak and saturates the transition. It is important to point out that, since the 3*s* and 6*p* sub-peaks are separated by U_p, we used this energy separation to calibrate the laser intensity in the focus of the beam (Figure 18).

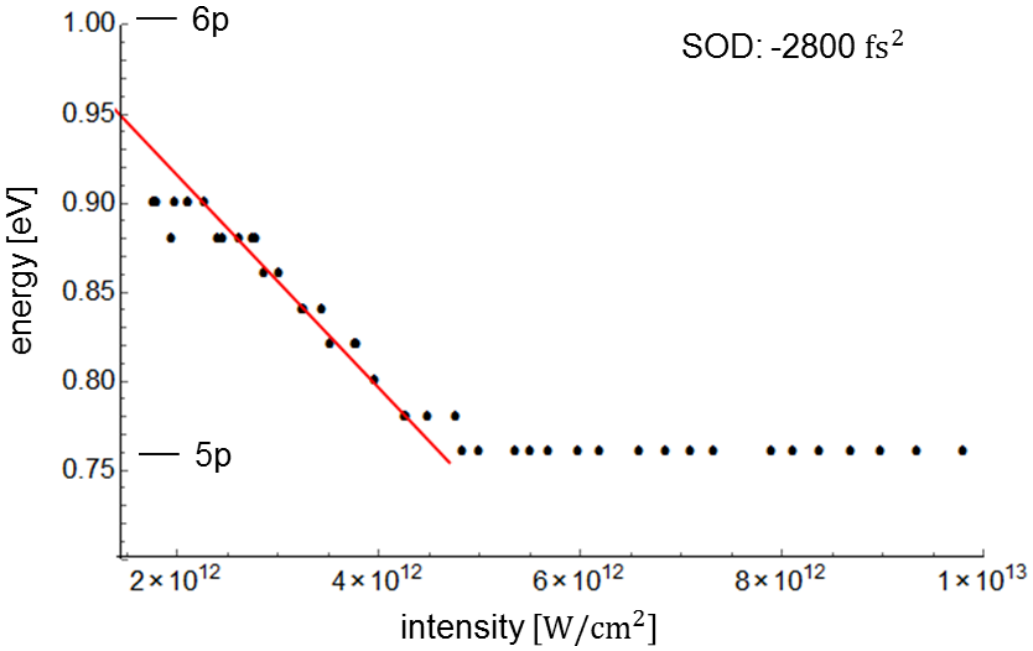

Figure 18. Experimental data showing the electron energy of the 3s peak maximum as a function of laser intensity. The red curve is the theoretically predicted peak position of the 3s peak (E_{3s} = $4\hbar\omega$ - E_I - U_p). Note that the 3*s* and 5*p* peaks merge at ≈ 4.7×10^{12} W/cm^2. The pulse duration is τ ≈ 150 fs^2.

Figure 19 displays integrations (FWHM) of the electrons in subpeaks 3*s* & 5*p* (blue), 6*p* (purple) and the entire ATI spectrum from 0 - 8 eV (gold). 3*s* and 5*p* are not distinguished for the above mentioned reason. Note that 5*p* and 6*p* saturate at different intensities and their saturations are chirp-dependent.

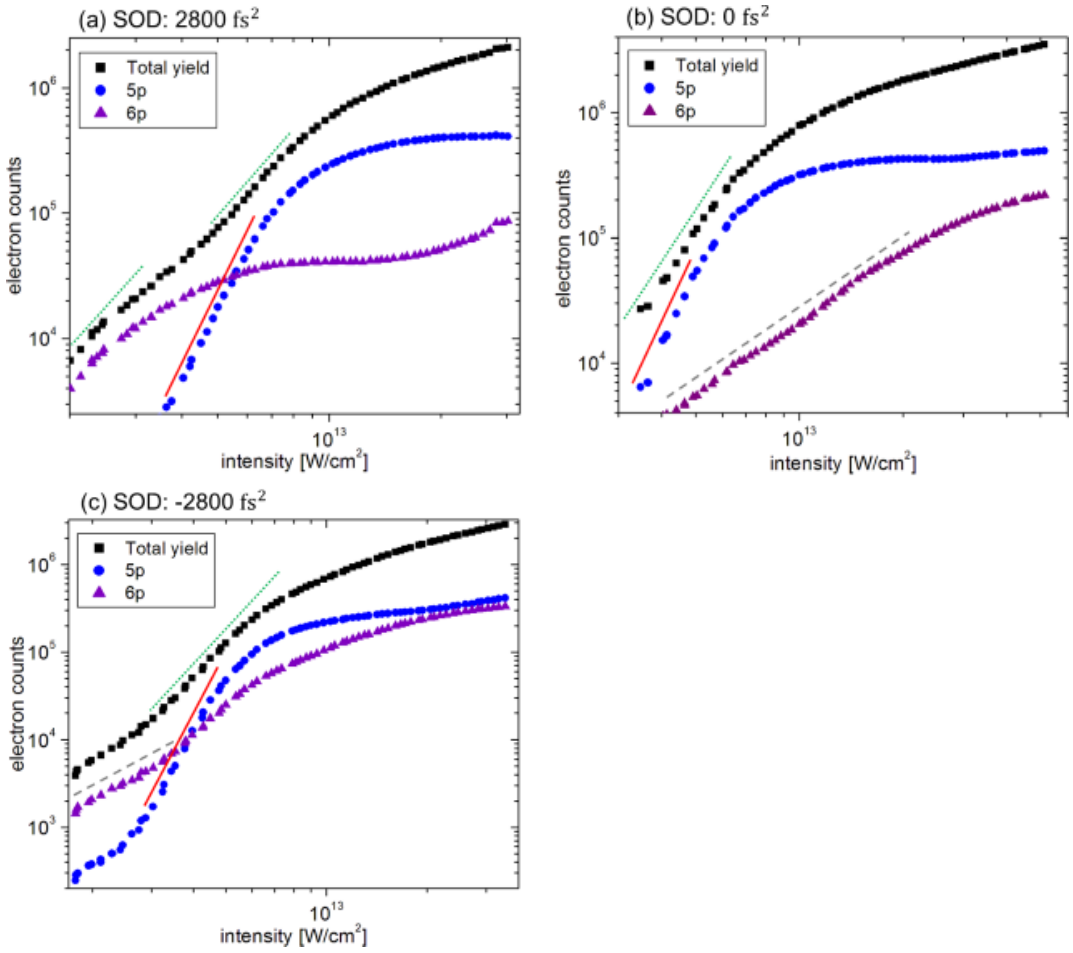

Figure 19. Electron yields for the total photo-electron spectra (black squares) and the 5*p* (blue circles) and 6*p* (purple triangles) peaks as a function of laser intensity. In each plot, the 5p and 6p peaks from the data in Figure 16 are integrated for ~FWHM of their width, while "Total yield" refers to an integration of the entire photo-electron spectrum (all orders) for a specific intensity. In each plot, the green dotted line refers to $K = 4$, the red solid line refers to $K = 6$ and the grey dashed line is the result of $K = 2$.

According to the perturbation theory of multiphoton absorption, 5*p* and 6*p* should have ionization yields that are proportional to the peak intensity I_0 to the 4th power ($Y \propto I_0^4$) or a slope of four on a log-log plot of the yield. The slope is defined as the *K* value for that transition (see subsection 4.4 Multiphoton Ionization) and would in this case be $K = 4$. Yet for zero and negative chirp, $K_{6p} \ll 4$. Moreover, $K_{5p} = 6$ for all three SOD values in

Figure 19. These abnormal slope dependences are largely masked in the overall yield (the gold curve) and would not be detected in an ion measurement of the sodium and laser interaction. The increased slope of 5*p* cannot be due to collective Penning or associative ionization since our Na vapor density, $\rho = 5.7\times10^{13}$ cm^{-3}, is too small for collisions to have a significant effect[36]. Additionally, for collisional ionization, we would expect an increased *K* for both 5*p* and 6*p* because of their similar spontaneous decay times (~1 μs) and Penning cross sections (~10^{-19} cm^2)[36]. The decreased slope of 6*p* cannot be accounted for by tunneling ionization because the Keldysh parameter at the over-the-barrier intensity is $\gamma = 3.98$. This tunneling parameter is also interesting because it indicates that the ionization of sodium with our pulse parameters remains a multiphoton process even passed the predicted saturation intensity[3]. If tunneling were a factor, we should expect a decrease in the slope of 5*p* also.

The difference between the intensity responses of the two energy states may be explained by the fact that as intensity increases 5*p* AC Stark shifts towards the three-photon resonance from the ground state (3*s*→→→|), while 6*p* shifts away from this resonance. Figure 20 shows the results of a simplified model demonstrating the effect of replacing the static three-photon detuning of the unperturbed atom, $\delta_s = 3\nu_0 - \omega_{3s,e}$, with the dynamic detuning, $\delta(t) = 3\nu(t) - \omega_{3s,e} - E^{(2)}(t)/\hbar$, in the Lorentzian line-shape function of the final excited state (see section 8. Resonance Sampling Model).

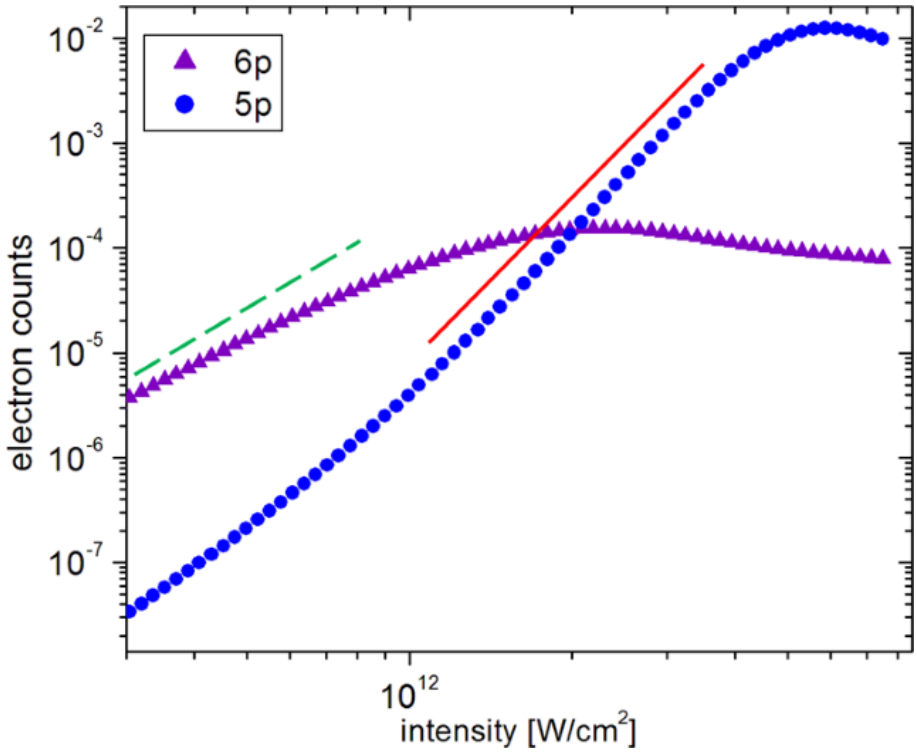

Figure 20. Results of the Resonance Sampling model for three photon absorption by 5p and 6p levels as a function of the pulse peak intensity. The green dashed line has a slope K = 3, and the red solid line has a slope K = 5.

Here $E^{(2)}(t) \propto$ (intensity of pulse envelope) and $\nu(t) = \nu_0 + \alpha \cdot t$, where α, the chirp parameter (see section 3.3.2 Chirped Pulse and Second Order Dispersion), is set to zero. We see that the Stark shift alone is able to reproduce qualitatively the increase of K_{5p} and decrease of K_{6p}. At the lowest intensity, both 5p and 6p have a K value of 3 which is the expectation for three photon absorption. The slope K of 5p increases with intensity until the resonance condition is satisfied around 5×10^{12} W/cm^2. Contrarily, the slope of 6p always decreases from its maximum value of 3, indicating that 5p is enhanced and 6p is attenuated by the same mechanism (Figure 21 (a) and (b)). This is a remarkable result since this model does not account for any interference dependent phenomena. Moreover, this dual mechanism may be used for the selective excitation of energy levels (Figure 21 (c)).

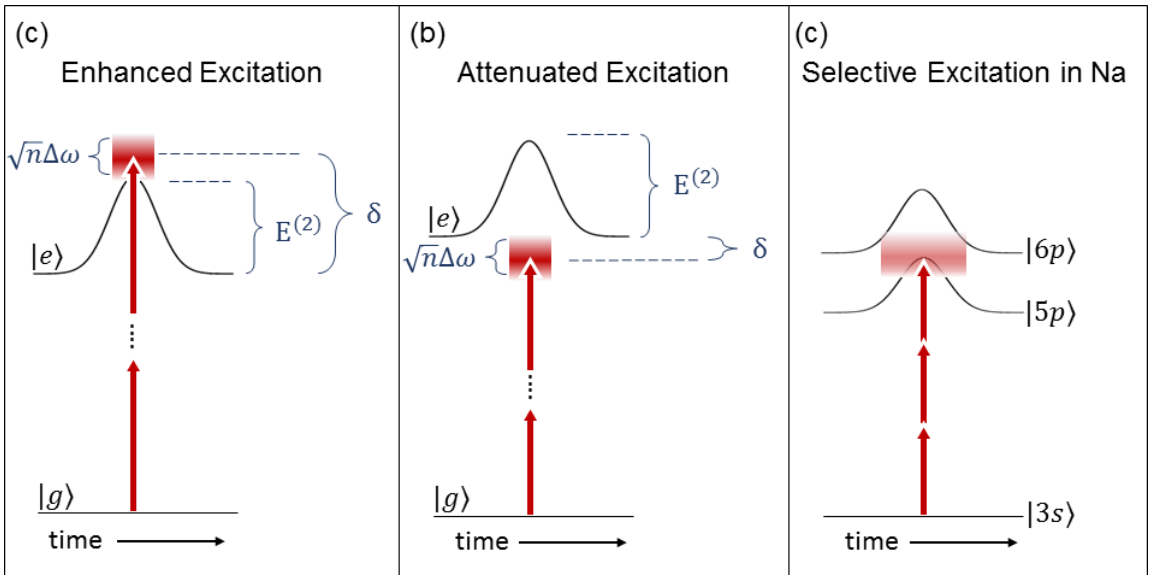

Figure 21. A graphical depiction of enhanced and attenuate excitation due to the AC Stark shift of the excited state. An unchirped Gaussian pulse is implicitly assumed. (a) shows the excited state being Stark shifted into resonance, while (b) shows the excited state being Stark shifted out of resonance. (c) visualizes how the 5*p* state of sodium may be selectively excited.

Note, however, that the dynamic detuning $\delta(t)$ is a function of two time dependent variables, the AC Stark shift and the time dependent frequency. If this detuning really is the variable responsible for the change in the ionization rate, we should see that modifications to the spectrum can also produce a simultaneous enhancement of ionization from *5p* and an attenuation of *6p*.

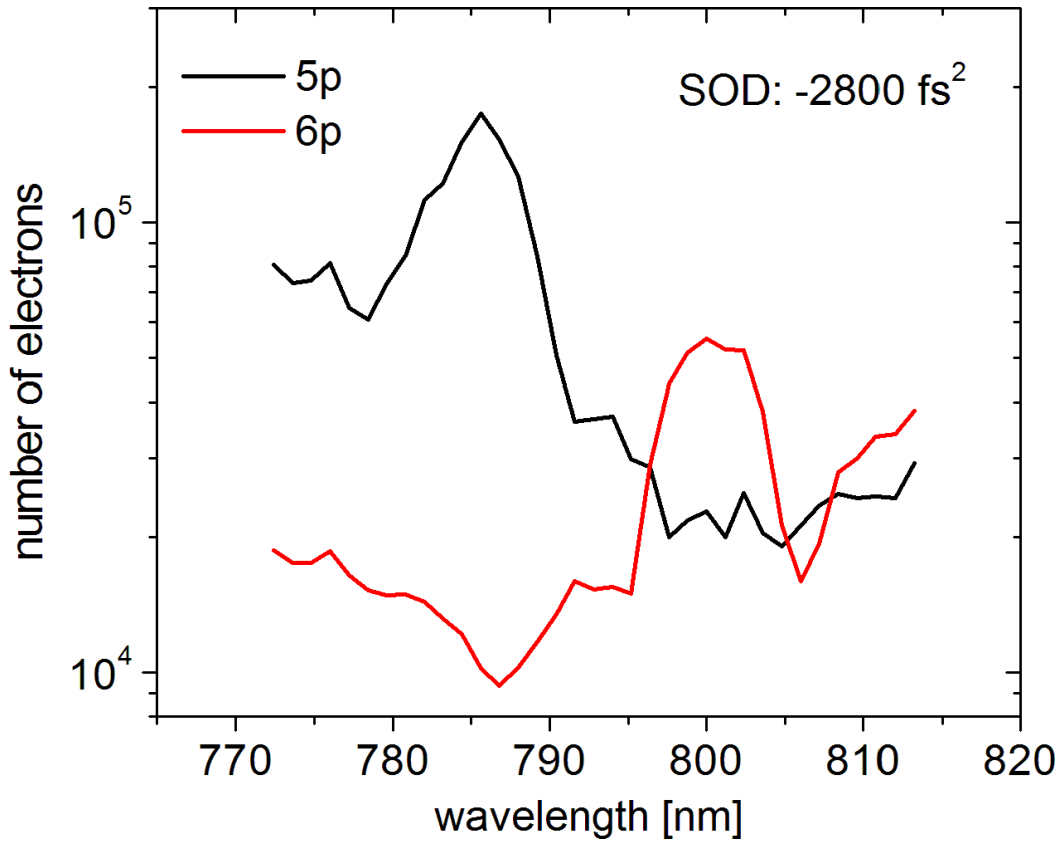

Figure 22. Experimental results of a Spectral Scan taken at a SOD of -2800 fs^2. The electrons in the *5p* and *6p* peaks are integrated at FWHM to produce each data point. The plot therefore shows ionization as a function of the block position. Each peak is enhanced when the average spectral detuning is decreased and attenuated when the average spectral detuning increased.

By performing a Chirp Scan, we were able to modify the effective multiphoton detuning for various levels and demonstrate selective excitation of *5p* and *6p* (see Figure 22). Blocking the higher optical frequencies increases the average detuning of the pulse from the *6p* level and decreases the detuning from *5p*, while blocking lower frequencies has the opposite effect. Indeed, changing the detuning through either modifications to the spectrum or the intensity show similar effects on the populations of *5p* and *6p*. Blocking the higher frequencies enhances the *5p* ionization signal and attenuates ionization from

the *6p* level. Contrarily, blocking lower frequencies attenuates the *5p* signal and enhances *6p* ionization.

Figure 23 displays a Chirp Scan of sodium at a constant intensity of $I_o = 5.5\times10^{12}$ W/cm^2. This, of course, requires that the pulse energy increases with the magnitude of the SOD. Note that the enhancement of 5*p* is chirp independent.

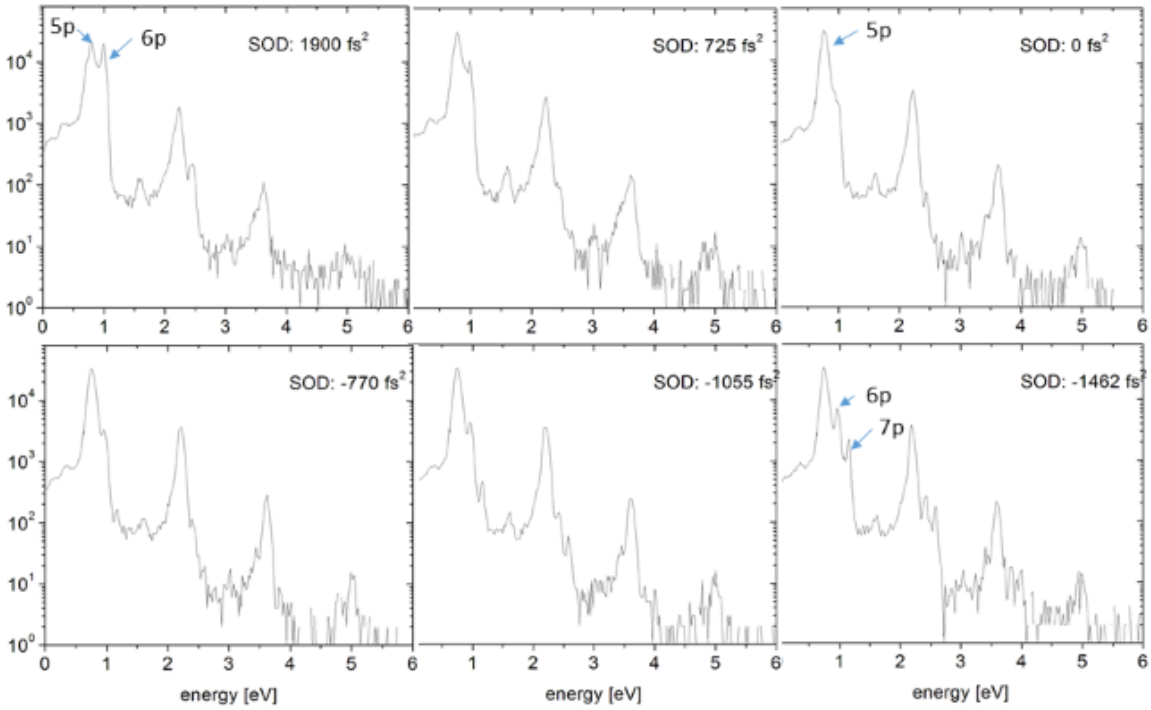

Figure 23. Selected photoelectron spectra at SOD values of 1900 fs^2, 725 fs^2, 0 fs^2, -770 fs^2, 1055 fs^2 and -1462 fs^2 from a chirp scan at $I_o = 5.5\times10^{12}$ W/cm^2. 5*p* shows chirp independence since it is shifted into resonance at the peak of the pulse. While 6*p* shows a minimum around zero dispersion. 7*p* only appears for dispersion values.

6*p* and 7*p* show dramatic asymmetry with respect to SOD. Both states begin ionizing for sufficiently large negative dispersion (SOD = -770 fs^2) indicating a common mechanism. In fact, the three-photon resonance (3s→→→|) for the highest energy photons in the laser bandwidth sits above 7*p*, while the same resonance for the smallest energy photons sits below 6*p*. Negative chirp requires that high energy photons lead the

pulse. Thus, the three-photon energy $3\hbar\nu(t)$ decreases with time and samples both the 6*p* and 7*p* resonances on the rise of the pulse. Efficient excitation and ionization can then occur but only for a short period of time. For positive chirp, 6*p* shows a relatively high ionization yield rivaling that of 5*p*. But this is true only for a narrow range of SOD between 900 and 2900 fs^2. The high yield of 6*p* in this "SOD window" can be explained by the fact that the three-photon resonance energy $3\hbar\nu(t)$ increases together with the AC Stark shift $E^{(2)}(t)$ such that the detuning ($\delta(t) = \delta_s$) is constant on the rising edge of the pulse. This constant detuning restores the expected multiphoton order K_{6p}= 4 and enhances the excitation (Figure 19 (a)). Nonetheless, 6*p* saturates at this intensity while the yield of 5*p* continues to increase (Figure 19 (a)). The femtosecond pulses used in this experiment do not satisfy the adiabaticity criterion[37] and the results of this experiment are inherently nonadiabatic[20]. Therefore, rapid adiabatic passage (RAP)[37,38] and Stark chirped rapid adiabatic passage (SCRAP)[39] mechanisms do not apply here.

Note that in Figure 23, at zero second order dispersion, 5*p* is selectively enhanced with negligible ionization from other excited states. This fact is more clearly seen on a linear plot of the same measurement shown in Figure 23 at zero chirp (see Figure 24).

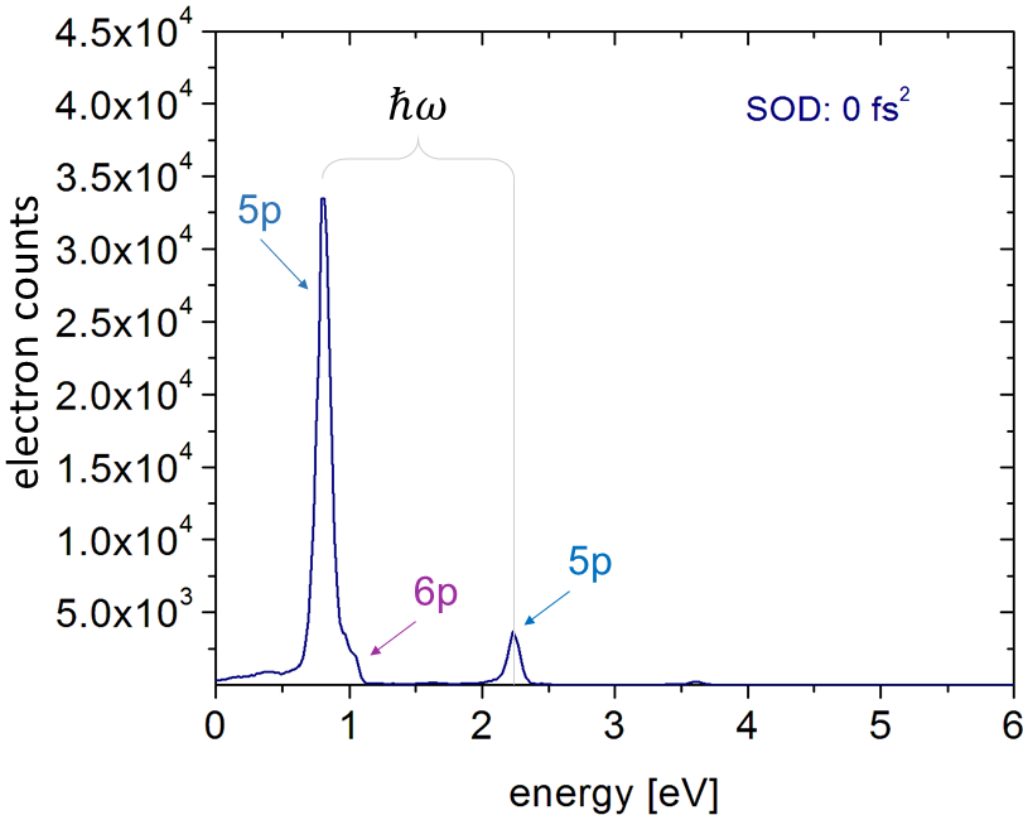

Figure 24. Photoelectron spectra of sodium for zero chirp and a laser intensity of 5.5×10^{12} W/cm^2. The two peaks labeled 5*p* are approximately one photon apart. 83% of the electrons can be attributed to ionization from 5*p*.

At intensities above the 5*p* saturation, significant broadening of 5*p*, 6*p* and 7*p* occurs. The same effect is seen in Figure 16 (a), (c) and (e) as red coloring of the 3D surface plots. This broadening may be the result of faster ionization (smaller Δt) from the excited state according to the uncertainty principle ($\Delta E \cdot \Delta t \sim \hbar/2$). However, more investigation into the nature of the broadening is warranted.

8. RESONANCE SAMPLING MODEL

Here we seek a simple qualitative model that can predict the abnormal slope dependences seen in our data as atomic states Stark-shift into and out of resonance. Lowest order perturbation theory (LOPT) is a greatly simplified model that predicts for an *n* photon absorption, the rate *R*(t) at which this process occurs is proportional to the laser intensity to the n^{th} power ($R(t) = \sigma_n(\nu)\, I^n$). The probability for the n^{th} order excitation is then:

$$P_n(t) = \int_{-\infty}^{t} R(t')dt' \tag{8.1}$$

where the multiphoton cross section[26] for excitation from an initial state $|g\rangle$ is

$$\sigma_n(\nu) = \left(\frac{2}{c\epsilon_0\hbar}\right)^n \left| \sum_{a_1 \cdots a_{n-1}} \frac{\langle f|x|a_{n-1}\rangle \cdots \langle a_1|x|g\rangle}{\left(\omega_{a_{n-1}} - (n-1)(\nu - i\gamma_{n-1})\right) \cdots \left(\omega_{a_1} - \nu + i\gamma_1\right)} \right|^2 2\pi\rho_f(\omega_{fg} - n\nu). \tag{8.2}$$

Here, γ_j represents the decay rate for the *j*th energy level, a_j is the *j*th intermediate state, and $\rho_f(x)$ is the Lorentzian density of states for the final state $|f\rangle$. *The main point of the Resonance Sampling Model* is to replace the static detunings ($\delta_{ij} = \omega_{ij} - n\nu$) in equation 8.2 with the dynamic detunings ($\delta_{ij} = \omega_{ij} + E^{(2)}(t) - n\nu$) for each level, and then average the cross section $\sigma_n(\nu)$ over the time dependent frequency spectrum of the laser. In calculating the rate using LOPT, four simplifying approximations are made.

1. Slow varying amplitude approximation or continuous wave radiation
2. Rotating wave approximation (RWA)
3. The ground (initial) state is not depleted
4. No Stark shifts/splits (Rabi Splitting, AC Stark effect)

For the pulses in our experiment, *approximations 1* and *2* are valid. Concerning *approximation 1*, note that for a simple Gaussian pulse:

$$I(t) = I_0 e^{-\frac{at^2}{\tau^2}} \mathrm{Cos}(\nu_0 t) \tag{8.3}$$

where $a = 4Log(2)$ satisfies the FWHM condition. Now we want to know how the magnitude of the change in the pulse amplitude compares to the change in its sinusoidal oscillation. The inflection point of the exponential envelope is located at $t_{in} = \tau/\sqrt{2a}$ and the first derivative of $I(t)$ at t_{in} is:

$$\frac{dI(t_{in})}{dt} = I_0 e^{-\frac{1}{2}} \left(-\frac{1}{t_{in}} \mathrm{Cos}(\nu_0 t_{in}) - \nu_0 \mathrm{Sin}(\nu_0 t_{in}) \right) \tag{8.4}$$

For a pulse duration τ = 56 fs and a laser period of T = 2.66 fs, we see that the rate-of-change in the intensity due to the pulse envelope ($1/t_{in} = 4.2\times10^{13}$ s^{-1}) is much smaller than the change due to oscillations ($\nu = 2.4\times10^{15}$ s^{-1}) and thus can be neglected. Nonetheless, for pulsed radiation, one must average the absorption cross-section $\sigma_n(\nu)$ over the normalized spectral distribution of the laser. Care must be taken, since the effective spectrum changes (increases$\times\sqrt{n}$) in the case of a multiphoton transition. More on averaging over the laser bandwidth will be discussed later in this section.

For *approximation 2* (RWA), simply note that for a multiphoton resonance ($\omega_{fi} \approx n\nu$) the "exact" rate contains a term that is inversely proportional to ($\omega_{fi} - n\nu$) corresponding to a contribution from slowly rotating complex wave and a term that is inversely proportional to ($\omega_{fi} + n\nu$) corresponding to a contribution from the fast rotating wave. And since:

$$\frac{1}{\omega_{fi} - n\nu} \gg \frac{1}{\omega_{fi} + n\nu}. \tag{8.5}$$

we expect the contribution from the slow rotating wave to dominate. There also exist other terms which are a mixture of contributions from both fast and slow rotating waves. These cross-terms are also much smaller than the contribution due solely to the slow rotating wave. However, the exact expression for the rate is rather large even for a two photon process (n = 2) and is visually cumbersome to display here. Appendix B contains Mathematica 10 code which prints out the complex amplitude for the two photon absorption into 4*s* (sodium, Na) obtained using only the slow varying amplitude approximation. Squaring this function and taking the time derivative produces the two photon absorption rate.

Approximation 3 is usually rectified by solving a system of rate equations which allows the ground state to be depleted. Let N_i and N_f be the electron number density in the initial and final states. Then for a multiphoton transition between these two states we have:

$$\frac{dN_i}{dt} = -R(t)(N_i - N_f) \tag{8.6}$$

$$\frac{dN_f}{dt} = R(t)(N_i - N_f) \tag{8.7}$$

Subtracting the these two derivatives yields:

$$\frac{d}{dt}(N_i - N_f) = -2R(t)(N_i - N_f) \tag{8.8}$$

whose solution is:

$$\begin{aligned}\left(N_i - N_f\right) &= \left(N_{i0} - N_{f0}\right) Exp\left(-2\int_{-\infty}^{t} R(t')dt'\right) \\ &= Exp\left(-2\int_{-\infty}^{t} R(t')dt'\right)\end{aligned} \tag{8.9}$$

if at t = -∞, all of the electron population is in the initial state (N_i = 1 and N_f = 0). Now, using the conservation relation N_i = 1-N_f and solving for the population in the final state we get:

$$N_f = \frac{1}{2}\left(1 - Exp\left(-2\int_{-\infty}^{t} R(t')dt'\right)\right) \tag{8.10}$$

Finally, the omission of the AC Stark shift, $E^{(2)}(t)$, in *approximation 4* can be compensated for by including the dynamic detuning, $\delta_f(t) = \omega_{fg} + E_f^{(2)}(t) - n\,v(t)$, phenomenologically into the density of states variable. In other words, the static detuning, $\delta' = \omega_{fg} - n v_0$, in the Lorentzian density ρ(x) is substituted by the dynamic detuning,

$$\rho_f\left(\delta' \to \delta_f(t)\right) = \frac{1}{\pi}\frac{(\gamma_f/2)}{\left(\omega_{fg} + E_f^{(2)}(t) - n\,v(t)\right)^2 + \left(\frac{\gamma_f}{2}\right)^2}. \tag{8.11}$$

At this point, it is important to mention that all of the atomic states undergo a dynamic Stark shift. For this reason, the denominator in the absorption cross-section Eq. 8.2 ensures that the dynamic detuning must be included for *all* the intermediate states as well as the final excited state.

As an example in sodium (Na) vapor, consider a three photon absorption to the 6*p* state in with a laser field only slightly red-detuned from a two photon resonance between the 3*s* ground state and the 4*s* second excited state (see section 5. Properties of Sodium

Atoms…, Figure 15). To be more specific, the laser spectrum will have a broad Gaussian profile centered on 800 nm (1.55 eV). In this scenario, there is only one quantum path that contains a near-intermediate resonance (3*s*→→4*s*→6*p*) and this pathway dominates the excitation process. The three photon cross-section can thus be approximated by:

$$\sigma_{6p}(t,\nu) \approx A\mu_{6p,4s}\mu_{4s,3p}\mu_{3p,3s}\rho_{6p}\left(\delta_{6p}(t,\nu)\right)\rho_{4s}\left(\delta_{4s}(t,\nu)\right)\rho_{3p}\left(\delta_{3p}(t,\nu)\right), \quad (8.12)$$

where

$$A = \frac{(2\pi)^3}{\gamma_{3p}\gamma_{4s}}\left(\frac{2}{c\epsilon_0\hbar}\right)^3 \quad (8.13)$$

$$\rho_{3p}\left(\delta_{3p}(t,\nu)\right) = \frac{1}{\pi}\frac{(\gamma_{3p}/2)}{\left(\omega_{3p,3s} + E_{3p}^{(2)}(t) - \nu\right)^2 + \left(\frac{\gamma_{3p}}{2}\right)^2}.$$

$$\rho_{4s}\left(\delta_{4s}(t,\nu)\right) = \frac{1}{\pi}\frac{(\gamma_{4s}/2)}{\left(\omega_{4s,3s} + E_{4s}^{(2)}(t) - 2\,\nu\right)^2 + \left(\frac{\gamma_{4s}}{2}\right)^2}.$$

$$\rho_{6p}\left(\delta_{6p}(t,\nu)\right) = \frac{1}{\pi}\frac{(\gamma_{6p}/2)}{\left(\omega_{6p,3s} + E_{6p}^{(2)}(t) - 3\nu\right)^2 + \left(\frac{\gamma_{6p}}{2}\right)^2}.$$

and $\mu_{j,k} = e\langle j|x|k\rangle$ represents the dipole moment between states *j* and *k*. Thus the absorption rate from 3*s* to 6*p* for a laser frequency ν is:

$$R_{6p}(t,\nu) \approx \sigma_3(t,\nu)I(t)^3. \quad (8.14)$$

This rate is applicable only to the laser frequency *ν* and must be integrated over the time-dependent multiphoton bandwidth (see section 3.3.3 Multiphoton Pulse Duration and Bandwidth) at each moment in time using the normalized spectrum (FWHM)

$$f(t,\nu) = \frac{\tau}{\sqrt{4\pi n\, Ln(2)}} e^{-\frac{(\nu_0+\alpha t-\nu)^2\tau^2}{4n\, Ln(2)}}. \tag{8.15}$$

where τ is the chirp dependent pulse duration (Eq. 3.22). Equation 8.15 is a normalized Wigner-Ville quasiprobability distribution[40] of Eq. 3.23. Therefore, we obtain an average (weighted) transition rate

$$\bar{R}_{6p}(t) = \int_{-\infty}^{\infty} f(t,\nu) R_{6p}(t,\nu)\, d\nu \tag{8.16}$$

which may be plugged into Eq. 8.10 ($R(t') \rightarrow \bar{R}(t')$) to obtain the population of the final state N_{6p}.

9. RESONANCE SAMPLING APPLICATIONS AND OUTLOOK

The ability to selectively excite Freeman resonances has important implications for remote sensing and coherent frequency generation. Air is composed of roughly 78% nitrogen gas (N_2), 21% oxygen gas (O_2) and 1% argon (Ar). If one would like to detect the presence of another molecule (i.e. nitric oxide), it is necessary to find a dynamic resonance that is not shared by the dominant air constituents N_2, O_2 and Ar. By dynamically shifting the air molecules away from an integer multiphoton resonance and the target molecule into an integer multiphoton resonance, selective REMPI (ionization) of the target molecule may be achieved. REMPI in molecules and atoms has been exploited using the RADAR REMPI technique for flame combustion analysis, plasma diagnosis[13,41,42] and remote sensing[43]. Our work is complementary to RADAR REMPI.

Additionally, the large three photon Rabi coupling generated in our experiments leads to the generation of dipole radiation between the 3*s* ground state and the 5*p* Freeman resonance state. However, these higher frequency photons could be reabsorbed if most of the sodium atoms are in any state other than 5*p*. Solving the time-dependent Schrodinger equation (see Appendix A for code), we see that a transient population inversion can occur when the 5*p* state Stark shifts into a three photon resonance (see Figure 25) which allows for the possibility of creating gain at the transition frequency by the propagation of the laser.

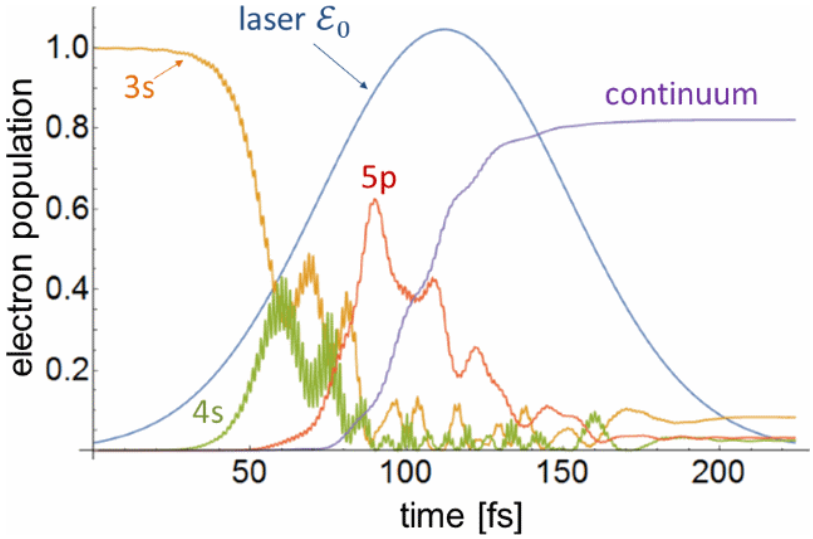

Figure 25. A numerical time-dependent Schrodinger equation simulation of a linearly polarized 56 fs laser pulse interacting with a sodium atom initially in the 3*s* ground state. The atom experiences a transient population inversion into the 5*p* state which peaks at 62% occupation and last for ~26 fs. Ionization then depletes the system.

Figure 26 shows the effect of transient dipole radiation corresponding to the simulation in Figure 25.

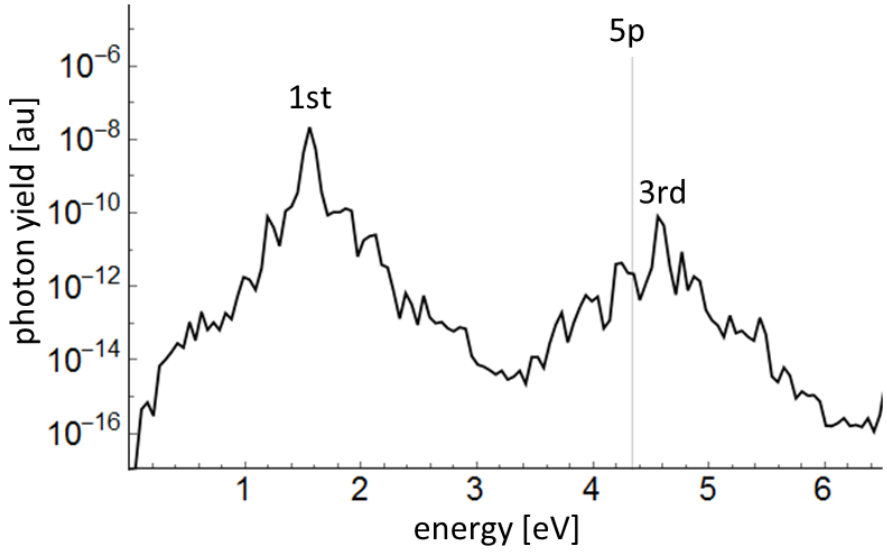

Figure 26. The radiation spectra for the corresponding simulation in Figure 25. The 1st and 3rd harmonics are located at 1.55 eV and 3.65 eV respectively. Radiation from the 5p→3s transition is marked by a vertical line at 4.34 eV.

10. CONCLUSION

In the strong field regime, coherent control of atomic state population can be hampered if the dynamic (AC) Stark shifts are not taken into account. We show experimentally that we are able to control atomic energy level population by varying the laser pulse intensity, chirp and spectral composition. It was shown in sodium that enhancement of the ionization yield from the specific Rydberg levels 5*p,* 6*p* and 7*p* occurs when these levels are in multiphoton resonance with the laser field. At low intensities 6*p* was selectively excited, because the laser field was tuned to a three photon resonance with this level. More importantly selective enhancement of 5*p* was attained at high intensities (strong field regime) approaching the saturation intensity.

We developed a model, termed Resonance Sampling (RS), which qualitatively describes the excitation dynamics as a function of the dynamic detuning $\delta(t)$ of the laser field from the resonant levels. It was shown through RS that the selective enhancement of 5*p* excitation involves the AC Stark shift of this state into resonance at the peak of the pulse. In contrast, the population of 6*p* is attenuated as it shifts out of resonance at the peak intensity. These diverging effects for the two states result in a selectively enhanced excitation of 5*p*. Moreover, the larger the positive detuning away from the unperturbed 5*p* state is, the larger the enhancement of 5*p* excitation. This is a startling effect, because it is the exact opposite of what is expected in the weak field regime.

Numerically solving the time dependent Schrodinger equation reveals that this selective excitation could result in population inversion of the atomic ensemble prior to

the efficient ionization of the atom, and leads to the transient generation of the third harmonic.

Our ability to selectively excite Rydberg levels may lead to remote sensing applications such as RADAR REMPI where selective excitation is required prior to ionization. Additionally, the generation of low order harmonics in the forward beam direction may also become a useful tool for gas characterization.

REFERENCES

1 Freeman, R. *et al.* Above-Threshold Ionization With Subpicosecond Laser Pulses. *Physical Review Letters* **59**, 1092 (1987).

2 Hertlein, M. P., Bucksbaum, P. H. & Muller, H. Evidence For Resonant Effects In High-Order ATI Spectra. *Journal Of Physics B: Atomic, Molecular And Optical Physics* **30**, L197 (1997).

3 Potvliege, R. & Vučić, S. Stark-Shift Induced Resonances In Multiphoton Ionization. *Physica Scripta* **74**, C55 (2006).

4 Held, B., Mainfray, G., Manus, C., Morellec, J. & Sanchez, F. Resonant Multiphoton Ionization Of A Cesium Atomic Beam By A Tunable-Wavelength Q-Switched Neodymium-Glass Laser. *Physical Review Letters* **30**, 423-426 (1973).

5 Chang, C. & Stehle, P. Theory Of Resonant Multiphoton Ionization. *Physical Review Letters* **30**, 1283 (1973).

6 Mittleman, M. H. In *Introduction To The Theory Of Laser-Atom Interactions* 153-231 (Springer, 1993).

7 Mulser, P. & Bauer, D. *High Power Laser-Matter Interaction*. Vol. 238 (Springer Science & Business Media, 2010).

8 Ishikawa, K. L., Schiessl, K., Persson, E. & Burgdörfer, J. Fine-Scale Oscillations In The Wavelength And Intensity Dependence Of High-Order Harmonic Generation: Connection With Channel Closings. *Physical Review A* **79**, 033411 (2009).

9 Kopold, R., Becker, W., Kleber, M. & Paulus, G. Channel-Closing Effects In High-Order Above-Threshold Ionization And High-Order Harmonic Generation. *Journal Of Physics B: Atomic, Molecular And Optical Physics* **35**, 217 (2002).

10 Corkum, P. B. Plasma Perspective On Strong Field Multiphoton Ionization. *Physical Review Letters* **71**, 1994-1997 (1993).

11 Dogariu, A., Michael, J. B., Scully, M. O. & Miles, R. B. High-Gain Backward Lasing In Air. *Science* **331**, 442-445 (2011).

12 Traverso, A. J. *et al.* Coherence Brightened Laser Source For Atmospheric Remote Sensing. *Proceedings Of The National Academy Of Sciences* **109**, 15185-15190 (2012).

13 Shneider, M. N. & Miles, R. B. Microwave Diagnostics Of Small Plasma Objects. *Journal Of Applied Physics* **98**, 033301 (2005).

14 Faisal, F. & Moloney, J. Time-Dependent Theory Of Non-Hermitian Schrodinger Equation: Application To Multiphoton-Induced Ionisation Decay Of Atoms. *Journal Of Physics B: Atomic And Molecular Physics* **14**, 3603 (1981).

15 Knight, P. AC Stark Splitting Of Bound-Continuum Decays. *Journal Of Physics B: Atomic And Molecular Physics* **12**, 3297 (1979).

16 Lambropoulos, P. *et al.* In *Thirteenth International Conference On Atomic Physics (ICAP-13).* 499-512 (AIP Publishing).

17 Nicklich, W. *Et Al.* Above-Threshold Ionization Of Cesium Under Femtosecond Laser Pulses: New Substructure Due To Strongly Coupled Bound States. *Physical Review Letters* **69**, 3455 (1992).

18 Lagattuta, K. Above-Threshold Ionization Of Atomic Hydrogen Via Resonant Intermediate States. *Physical Review A* **47**, 1560 (1993).

19 Clow, S. D., Trallero-Herrero, C., Bergeman, T. & Weinacht, T. Strong Field Multiphoton Inversion Of A Three-Level System Using Shaped Ultrafast Laser Pulses. *Physical Review Letters* **100**, 233603 (2008).

20 Trallero-Herrero, C., Cardoza, D., Weinacht, T. & Cohen, J. Coherent Control Of Strong Field Multiphoton Absorption In The Presence Of Dynamic Stark Shifts. *Physical Review A* **71**, 013423 (2005).

21 Trallero-Herrero, C., Clow, S. D., Bergeman, T. & Weinacht, T. Strong Field Coherent Control Of Atomic Population Transfer. *Journal Of Physics B: Atomic, Molecular And Optical Physics* **41**, 074014 (2008).

22 Bayer, T., Wollenhaupt, M., Sarpe-Tudoran, C. & Baumert, T. Robust Photon Locking. *Physical Review Letters* **102**, 023004 (2009).

23 Wollenhaupt, M., Bayer, T., Krug, M., Sarpe-Tudoran, C. & Baumert, T. In *Journal Of Physics: Conference Series.* 012053 (IOP Publishing).

24 Krug, M. *et al.* Coherent Strong-Field Control Of Multiple States By A Single Chirped Femtosecond Laser Pulse. *New Journal Of Physics* **11**, 105051 (2009).

25 Lee, S., Lim, J., Park, C. Y. & Ahn, J. Strong-Field Quantum Control Of 2+ 1 Photon Absorption Of Atomic Sodium. *Optics Express* **19**, 2266-2277 (2011).

26 Boyd, R. W. *Nonlinear Optics*. (Academic Press, 2003).

27 Delone, N. B. & Kraĭnov, V. P. *Multiphoton Processes In Atoms*. Vol. 13 (Springer Science & Business Media, 2000).

28 Keldysh, L. Ionization In The Field Of A Strong Electromagnetic Wave. *Sov. Phys. JETP* **20**, 1307-1314 (1965).

29 Baggesen, J. C. & Madsen, L. B. On The Dipole, Velocity And Acceleration Forms In High-Order Harmonic Generation From A Single Atom Or Molecule. *Journal Of Physics B: Atomic, Molecular And Optical Physics* **44**, 115601 (2011).

30 Firestone, R. B. *The Berkeley Laboratory Isotopes Project's*, <Http://Ie.Lbl.Gov/Education/Isotopes.Htm> (2000).

31 Contributors, W. *Sodium*, <Http://En.Wikipedia.Org/Wiki/Sodium> (2015).

32 En.Wikipedia, O. U. W. D. A. In *Photograph Taken 12/12/07* Vol. 4000x3000 (4.26 MB) (Ed Na (Sodium).Jpg) Sodium Metal From The Dennis S.K Collection. Selfmade Photo Taken 12/12/07 (Wikimedia, Wikimedia Commons, The Free Media Repository, 2007).

33 Original Pngs By Daniel Mayer, D., Traced In Inkscape By User:Stannered. In *Inkscape* (Ed Cubic-Body-Centered.Svg) Body-Centered Cubic Crystal Structure (Wikipedia, Wikimedia Commons, 2007).

34 Steck, D. A. Sodium D Line Data. *Report, Los Alamos National Laboratory, Los Alamos* **126** (2000).

35 Sansonetti, J. E. Wavelengths, Transition Probabilities, And Energy Levels For The Spectra Of Sodium (Nai–Naxi). *Journal Of Physical And Chemical Reference Data* **37**, 1659-1763, Doi:Doi:Http://Dx.Doi.Org/10.1063/1.2943652 (2008).

36 Lucatorto, T. B. & Mcilrath, T. J. Laser Excitation And Ionization Of Dense Atomic Vapors. *Appl. Opt.* **19**, 3948-3956, Doi:10.1364/AO.19.003948 (1980).

37 Malinovsky, V. S. & Krause, J. L. General Theory Of Population Transfer By Adiabatic Rapid Passage With Intense, Chirped Laser Pulses. *Eur. Phys. J. D* **14**, 147-155, Doi:10.1007/S100530170212 (2001).

38 Melinger, J. S., Gandhi, S. R., Hariharan, A., Goswami, D. & Warren, W. S. Adiabatic Population Transfer With Frequency-Swept Laser Pulses. *The Journal Of Chemical Physics* **101**, 6439-6454, Doi:Doi:Http://Dx.Doi.Org/10.1063/1.468368 (1994).

39 Yatsenko, L., Shore, B., Halfmann, T., Bergmann, K. & Vardi, A. Source Of Metastable H (2s) Atoms Using The Stark Chirped Rapid-Adiabatic-Passage Technique. *Physical Review A* **60**, R4237 (1999).

40 Diels, J.-C. & Rudolph, W. *Ultrashort Laser Pulse Phenomena*. (Academic Press, 2006).

41 Chng, T. L., Michael, J., Dogariu, A., Zaidi, S. & Miles, R. In *51st AIAA Aerospace Sciences Meeting Including The New Horizons Forum And Aerospace Exposition.*

42 Dogariu, A., Michael, J., Stockman, E. & Miles, R. B. In *Conference On Lasers And Electro-Optics.* CFU4 (Optical Society Of America).

43 Dogariu, A., Stein, C., Glaser, A. & Miles, R. B. 80240G-80240G-80249.

APPENDIX A:

TDSE INTEGRATION

$\text{auT} = 2.41888 \times 10^{-17}$; (* converts time to atomic units *)
$\text{auE0} = 5.1422 \times 10^{11}$; (* converts electric field to atomic units *)
$\tau = 56 \times 10^{-15}/\text{auT}$; (*Transform limited pulse duration*)
$\text{SOD} = 0.\times 10^{-30}(\text{auT})^{-2}$; (*Second Order Dispersion*)
$\alpha = \dfrac{\text{SOD}}{(\tau^4 + \text{SOD}^2)}$; (* chirp *)
$\tau\text{p} = \tau\sqrt{1 + (2\,\text{SOD}/\tau^2)^2}$; (*pulseduration*)
$\nu = 2\pi\dfrac{c}{\lambda}\text{auT}$; (* laser frequency *)
$\Delta\text{t} = \dfrac{2\pi}{2(\text{NumPhotons} * \nu)}$; (* time step *)
$\text{II} = 5.5 \times 10^{12}$; (* intensity *)
$\text{E0} = \text{Sqrt}\left[2.\left(\dfrac{\text{II} * 10000}{c * \epsilon 0}\right)\right]/\text{auE0}$;
$F = \text{Compile}\left[\{\{t, _{\text{Real}}\}\}, \text{E0} * \text{Exp}[-(t/\tau\text{p})^2]\text{Cos}[\nu * t + \alpha * t^2]\right]$;
$\mu\text{t} = \text{SparseArray}[.5\Delta\text{t} * \mu]$; (* square matrix of dipole moments *)
$\mu\text{M}[\text{t\_}] := \text{Module}[\{\text{rabiM}, \psi\},$
$\psi = \text{SparseArray}\left[\text{DiagonalMatrix}\left[\text{Exp}[-(I * w) * t]\right]\right]$; (* w
$= \text{vector of energy levels} *)$
$\text{rabiM} = \text{Conjugate}[\psi].\mu\text{t}.\psi]$
$\text{a} = \text{Table}[0, \{\text{i}, \omega\text{L}\}];\ \text{a}\left[[1]\right] = 1$; (* probability amplitude *)
$\text{aList} = \text{Table}[0, \{\text{i}, \text{iTotal}\}, \{\text{j}, \omega\text{L}\}];$
$\text{efield} = \text{Table}[0, \{\text{i}, \text{iTotal}\}];$
$\text{t} = -\text{iTotal} * .5 * \Delta\text{t};$
$\text{Fe} = 0.00;$
$\text{Timing}[(* \text{Time propagation} *)$
Do[
$\text{Fe} = \text{F}[\text{t}];$
$\text{H} = \text{I} * \mu\text{M}[\text{t}]\text{Fe} + \sigma 1 * \text{Fe2};$
$\text{a} = \text{LinearSolve}[\text{IM} + \text{H}, (\text{IM} - \text{H}).\text{a}];$
$\text{t} = \text{t} + \Delta\text{t};$
$\text{aList}[[\text{i}]] = \text{a};$
$\text{efield}[[\text{i}]] = \text{F2}[\text{t}];$
$, \{\text{i}, \text{iTotal}\}]$
]
$\text{aListT} = \text{Transpose}[\text{aList}];$
$\text{aplot} = \text{Table}\left[\text{Abs}\left[\text{aListT}[[\text{j}]] * \text{Conjugate}\left[\text{aListT}[[\text{j}]]\right]\right], \{\text{j}, \omega\text{L}\}\right]$;

```
tim = Table[i * Δt, {i, iTotal}] * auT * 10^15;
IonY = 1 - Sum[aplot[[j]], {j, n7p}];
ListPlot[Transpose[{tim, aplot[[n3s]]}], Joined-> True]
```

APPENDIX B:

PROBABILITY AMPLITUDES

Clear[c4s, a3]
exp[ω1, ω2, t] ≔ Exp[−I(ω1 − ω2 − ν)t] + Exp[−I(ω1 − ω2 + ν)t]
(∗ derivative of amplitude for 3p state ∗)
$da3[t\_] := \left(\frac{I}{2}\right)$ Ω3s, 3exp[ω3, ω3s, t]c3s + $\left(\frac{I}{2}\right)$ Ω4s, 3exp[ω4s, ω3, t]c4s;
a3 = FullSimplify[Integrate[da3[t], t]](∗ amplitude for 3p state ∗)
dc3s[t_] := I/2 Ω3s, 3exp[ω3, ω3s, t]a3; (∗ derivative of amplitudes ∗)
dc4s[t_] := I/2 Ω4s, 3exp[ω4s, ω3, t]a3; (∗ derivative of amplitudes ∗)
c3s = Integrate[dc3s[t], t](∗ amplitude for 3s state ∗)
c4s = Integrate[dc4s[t], t](∗ amplitude for 4s state ∗)

APPENDIX C:

XENON PAPER

Intensity-Resolved Above Threshold Ionization of Xenon with Short Laser Pulses

N. A. Hart[1,*], J. Strohaber[1,2], G. Kaya[1], N. Kaya[1], A. A. Kolomenskii[1], H. A. Schuessler[1]

[1]Department of Physics, Texas A&M University, College Station, TX 77843-4242, USA

[2]Department of Physics**,** Florida A&M University, Tallahassee, Florida 32307, USA

Abstract: We present intensity-resolved above threshold ionization (ATI) spectra of xenon using an intensity scanning and deconvolution technique. Experimental data were obtained with laser pulses of 58 fs and a central wavelength of 800 nm from a chirped-pulse amplifier. Applying a deconvolution algorithm, we obtained spectra that have higher contrast and are in excellent agreement with characteristic 2 and 10 U_p cutoff energies contrary to that found for raw data. The retrieved electron ionization probability is consistent with the presence of a second electron from double ionization. This recovered ionization probability is confirmed with a calculation based on the PPT tunneling ionization model [Perelomov, Popov, and Terent'ev, Sov. Phys. JETP 23, 924 (1966)]. Thus, the measurements of photoelectron yields and the developed deconvolution technique allowed retrieval of more accurate spectroscopic information from the ATI spectra and ionization probability features that are usually concealed by volume averaging.

_____

I. INTRODUCTION

The focal volume of a laser beam contains a continuum of intensities that vary both radially and longitudinally with respect to the axis of propagation and range from zero to some peak intensity I_0. Each intensity provides a unique ion yield contribution depending on the probability of ionization, $P(I)$, and the volume occupied by the radiation at that intensity. This results in an averaging effect that ultimately reduces the intensity resolution of an experimental measurement [1]. This lack of resolution masks intensity dependent phenomena such as the ionization probability, AC Stark shifts and Rabi oscillations in the atomic energy levels [2]. It has been shown that ions can be distinguished according to their location in the laser focus from which they are produced [3]. But while higher ionization states A^{+n} have been observed in ion time-of-flight (TOF) measurements [1,3], to the best of our knowledge the explicit manifestation of photoelectrons specific to a charge state greater than one has not been observed. The difficulty of such detection follows from the fact that measuring devices are rarely able to determine the location within the focus that an electron originated from. Insufficient temporal resolution results in integration of the signal over the entire focal volume of the laser. For instance, distinguishing two electrons in a field-free region each with 1.5 eV of kinetic energy and a separation distance of 10 μm would require data acquisition electronics with 13 ps temporal resolution. However, fast data acquisition electronics have timing resolutions of a few hundred picoseconds.

Theoretical calculations for laser-matter interactions are typically carried out using plane waves of coherent radiation with some time-dependent amplitude modulation

[4,5], and the probability of ionization is determined after the interaction. Because, in practice, ionization experiments with short laser pulses record the ionization yield after the pulse has interacted with the target, and because experimental results are spatially averaged, theoretically determined ionization probabilities are artificially averaged for comparison with experiments. The need to compare with the more fundamental non-spatially averaged theoretical results has motivated the design of intensity-resolved experiments. In them, the goal is to remove the influence of the spatially varying intensity distribution from laser beam modes and isolate the result of a single intensity. Hansch and Van Woerkom [6] used a slit to collect ions from a small cross-section area of the laser focus. The novelty of their approach was that they varied the intensity in which the detected ions were born by changing the position of the slit along the z-axis relative to the laser focus. Walker et. al [7] coupled this measurement with an algorithm that removes the effect of radial variation in the laser intensity. This combined technique is known as Intensity Selective Scanning (ISS). Bryan et. al. [8] modified ISS by accounting for diffraction effects along the z-axis of the laser focus.

Goodworth et. al. [9] developed a deconvolution scheme which used discretized iso-intensity rings of the two dimensional cross-sections of the laser focus. An off axis slit aligned perpendicular to the z-axis determined the width of these cross-sections from which the ions were collected. The volume of each iso-intensity ring was represented by a matrix element $V_{n,s}$ where n indexes the z-axis position and s indexes the intensity of the ring. Deconvolution, to obtain a probability P_s, was carried out by an inverse matrix $V_{s,n}^{-1}$ multiplication of the yields Y_n from the z-scanned measurement: $P_s = V_{s,n}^{-1} Y_n$.

Other methods have employed purely experimental techniques to measure ions from an iso-intensity volume of the laser focus, which is confined in all three spatial dimensions. Schultze et. al. [10], and Strohaber and Uiterwaal [3] used an imaging TOF spectrometer to sort positive ions from the focus. Ions created at different locations within the focus arrive at a detector at different times. In their experiments, arrival times coupled with longitudinal and transverse measurements provide the ability to both reconstruct the spatial iso-intensity shells of the laser focus and extract intensity-resolved ionization probabilities from intensity scans.

Strohaber et. al. [11] introduced the multiphoton expansion (MPE) as an analytical deconvolution of the laser focal volume by solving the linear Volterra equation of the first kind. The solution for the ionization probability is represented by a power series of the intensity suggesting the name of this approach. The Volterra integral represented the total number of ions detected from an N-dimensional (N = 1, 2 or 3) volume within the focus. As such, this approach allows for the deconvolution of a variety of intensity scanning experimental schemes.

In the present work, we developed a generalized algorithmic technique to recover intensity-resolved above threshold ionization (ATI) energy spectra using photoelectrons; additionally, this technique may also be used for other spatially averaged data. The technique involves obtaining ATI measurements using short laser pulses of different peak intensities and employing a deconvolution algorithm to remove the blurring effect of the spatially varying intensities. The results of this procedure revealed the presence of

an electron from a second ionization, and an unanticipated and unreported shift in the cutoff energies.

II. DISCRETE DECONVOLUTION AND REGULARIZATION

The measured ionization yield of an atom $Y(I_0)$ can be expressed as a convolution of the ionization probability per unit volume $P(I)$ and the derivative of the volume $V(I_0, I)$ enclosing all intensities greater than I up to a maximum or peak intensity I_0:

$$Y(I_0) = \int_0^{I_0} P(I) \left| \frac{\partial V(I_0, I)}{\partial I} \right| dI \quad , \tag{1}$$

where $V(I_0, I)$ contains the geometric information about the focal region being measured. Thus, it is implicitly dependent on the optics used and any apertures between the interaction region and the signal detector. The functional form of $V(I_0, I)$ in 1, 2, and 3 dimensions is given in Strohaber et. al. [11].

To deconvolve the ionization probability $P(I)$ from Eq. (1), the experiment must be repeated more than once using different peak intensities. Therefore, we introduce the notation I_n to denote the peak intensity of the laser beam in the n-th experiment. We will now construct a numerical approximation of Eq. (1). Note that the magnitude of both $V(I_n, I)$ and its I derivative become infinite as I approaches zero. Therefore the lower limit of Eq. (1) is computationally impractical, and the interval of integration will need to be truncated by a parameter $\delta I << I_n - \delta I$:

$$Y(I_n) = \int_0^{\delta I} P(I) \left| \frac{\partial V(I_n, I)}{\partial I} \right| dI + \int_{\delta I}^{I_n} P(I) \left| \frac{\partial V(I_n, I)}{\partial I} \right| dI$$
$$\approx \int_{\delta I}^{I_n} P(I) \left| \frac{\partial V(I_n, I)}{\partial I} \right| dI. \quad (2)$$

As I_n increases, the integral over the interval [δI , I_n] more accurately approximates the full integral over [0 , I_n]. Since the ionization probability $P(I)$ tends to decay with decreasing intensity, this also reduces the introduced approximation error.

To estimate Eq. (2) numerically, we can discretize the integral using a Riemann sum. The integration interval is partitioned by introducing an ordered set of intensities $I_s \in \{I_1, I_2, ..., I_N\}$ such that $I_1 > I_2 > ... > I_N > \delta I$. Note that our choice of notation for I_n deliberately restricts the set of peak intensities at which we experimentally measure the yield $Y(I_n)$. Since $V(I_n, I_s)$ monotonically increases with decreasing I_s, the volume $V(I_n, \delta I)$ is also implicitly partitioned. We can therefore introduce differential volume elements $\Delta V = V_{n,s}$ for the set I_s at a peak intensity I_n to approximate Eq. (2).

$$\int_{\delta I}^{I_n} P(I) \left| \frac{\partial V(I_n, I)}{\partial I} \right| dI = \lim_{N \to \infty} \sum_{s=n}^{N} V_{n,s} P(I_s) \approx \sum_{s=n}^{N} V_{n,s} P(I_s). \quad (3)$$

$V_{n,s}$ and the corresponding Riemann sum can be defined in a number of different ways (midpoint rule, trapezoidal rule, Simpsons rule, etc…). However, any definition of $V_{n,s}$ must satisfy

$$\sum_{s=n}^{N} V_{n,s} = V(I_n, \delta I) \quad , \quad (4)$$

meaning that the sum of all differential volume elements must equal to the total volume enclosed by the smallest intensity δI. Moreover, to obtain a good approximation to Eq. (3) the condition $V_{n,s} << V(I_n, \delta I)$ should be satisfied for all s. We chose, for simplicity, to define $V_{n,s}$ by taking the difference between the volumes enclosed by two consecutive iso-intensity shells:

$$V_{n,s} \equiv \begin{cases} \left| V\left(I_n, I_{s+1}\right) - V\left(I_n, I_s\right) \right| \to s \geq n \\ 0 \to s < n \end{cases}. \tag{5}$$

This definition follows from the discrete first derivative of the volume:

$$\frac{\Delta V\left(I_n, I_s\right)}{\Delta I} \Delta I = \frac{V\left(I_n, I_s\right) - V\left(I_n, I_{s+1}\right)}{I_s - I_{s+1}} (I_s - I_{s+1}) \tag{6}$$

and is equivalent to taking a right Riemann sum.

If the indices n and s have the same dimensions $\left(n, s \in \{1, 2, ..., N\}\right)$, Eq. (3) produces a system of linear equations that can be expressed in matrix form as $\boldsymbol{Y} = \hat{V} \cdot \boldsymbol{P}$, where $\hat{V} \equiv V_{n,s}$ denotes the differential volume matrix, $\boldsymbol{P} \equiv \left(P\left(I_1\right), P\left(I_2\right), ..., P\left(I_N\right)\right)^T$ is the probability array and $\boldsymbol{Y} \equiv \left(Y\left(I_1\right), Y\left(I_2\right), ..., Y\left(I_N\right)\right)^T$ is the signal yield array. Solving for the ionization probability per unit volume, $\boldsymbol{P}$, we obtain:

$$\boldsymbol{P} = \hat{V}^{-1} \cdot \boldsymbol{Y} = (\hat{V}^T \hat{V})^{-1} \hat{V}^T \cdot \boldsymbol{Y} . \tag{7}$$

A one-dimensional example illustrating the construction of Eq. (7) is presented in Appendix A.

Since I_N would be the smallest element in the list of measured intensities, a free parameter $I_{N+1} \equiv \delta I$ must be chosen for the calculation of an outermost volume $V(I_n, I_{N+1})$ for all n (see Fig. 1). The choice of the free parameter $I_{N+1} = \delta I$ in Eq. (3) can be determined from $V_{N,N} = Y(I_N)/P(I_N)$, which assumes some knowledge of the probability $P(I_N)$. We note that for some simple atoms in the multiphoton regime, the probability $P(I_N)$ can be determined theoretically using perturbation theory [12]. It is known that the multiphoton yield at low intensities is proportional to the probability, since the highest intensity of the beam dominates the signal. We therefore determine δI by requiring that the derivatives of the probability and yield are equal at I_N, i.e. $\Delta P / \Delta I = \Delta Y / \Delta I_0$.

It is important to note that, in practice, the inversion in Eq. (7) is unstable with small variations in the yield $\boldsymbol{Y}$. However, by implementing a modified version of the variation minimization algorithms proposed by Le et. al. [13], and Chartrand and Wohlberg [14], we are able to introduce a regularization term to the right hand side of Eq. (7) to obtain the regularized probability $\bar{\boldsymbol{P}}_i$.

$$\bar{\boldsymbol{P}}_i = \left(\hat{V}^T\hat{V} - 2\beta\hat{M}_i\hat{\nabla}^2\right)^{-1}\hat{V}^T\boldsymbol{Y} \tag{8}$$

A more detailed discussion of the regularization algorithm, including the regularization term, $2\beta\hat{M}_i\hat{\nabla}^2$, and the iteration subscript i are discussed in Appendix B. The iteration

of Eq. (8) and its regularization term to find $\bar{\boldsymbol{P}}_i$ is hereafter referred to as the discrete deconvolution and regularization (DDAR) algorithm.

III. EXPERIMENTAL SETUP

The ATI apparatus is depicted in Fig. 2. Target xenon atoms were ionized with short laser pulses. A series of ionization measurements was taken for 120 different peak laser intensities ranging within $3\times10^{13}-8\times10^{14}\,\mathrm{W/cm^2}$. All other laser parameters, such as mode quality, pulse duration and spectral bandwidth were unchanged.

The Ti:Sapphire laser oscillator provides 20 fs mode-locked laser pulses at a repetition rate of 80 MHz. These pulses are seeded into a regenerative laser amplifier, which outputs 58 fs (measured by frequency resolved optical gating, GRENOUILLE 8-20, Swamp Optics, LLC) laser pulses at a repetition rate of 1 kHz, and a central wavelength of 800 nm. Since shorter pulses have a higher peak intensity for a given pulse energy, temporal compression of the laser pulses in the focus was achieved by maximizing the integrated photoelectron yield in the ATI apparatus by adjusting the grating compressor in the laser amplifier. The maximum pulse energy was approximately 0.8 mJ.

Laser pulses were detected before the half-wave plate of the attenuator by a photodiode, and the signal was used to trigger the data acquisition software. The attenuator consisted of a half wave plate that changed the polarization of the initially horizontally polarized light and a polarizing cube that filtered out vertically polarized light, while horizontally polarized light passed through. The orientation of the wave

plate was varied such that after the polarizing cube the desired intensity is achieved in the laser focus.

The vacuum chamber was filled with xenon gas of 99.999% purity (Advanced Specialty Gasses) through a variable leak valve. The xenon pressure (5×10^{-6} mbar) was three orders of magnitude higher than the background pressure in the ionization chamber. Because the ionization potential of water (12.61 eV) is roughly equal to that of xenon (12.15 eV), a large-surface-area vacuum feed-through, located on the time-of-flight (TOF) chamber, was chilled using liquid nitrogen to freeze out residual water molecules from the background vacuum. The laser beam was focused by a 20 cm achromatic lens. Ionized electrons were ejected along the polarization of the laser field in the direction of the microchannel plate (MCP) detector. The electrons travelled within a μ-metal TOF tube in a field-free region. Electrons from the entire focal volume of the laser were measured at the detector. The signals from the MCP were amplified by a high bandwidth Mini-Circuits ZKL-2 pre-amplifier before being registered by a FAST ComTec MCS6 multiscaler with 100 ps timing resolution. A power meter (PM) measured the average laser power, which is proportional to the average peak laser intensity in the focus.

The DDAR algorithm was written in Mathematica® and employed on an Intel i7 desktop computer having 16 GB of memory. The algorithm deconvolved the entire data set (a 19.0MB matrix of raw electron TOF spectra) in 0.824s.

IV. RESULTS

The electron ionization yield as recorded along the laser polarization is shown in Fig. 3. The saturation intensity is measured to be $I_{sat} = 1.2 \times 10^{14}\,\mathrm{W/cm^2}$. On a Log-Log plot the yield curve shows a slope of 5 for intensities less than I_{sat} and a slope of 3/2 for intensities greater than I_{sat}. The slope of 3/2 arises from volumetric integration of the electrons ionized from all intensities in the Gaussian beam. As the peak intensity $I_0 \equiv I(r = 0)$ increases, the total volume enclosed by an intensity $I(r > 0) < I_0$ grows as $I_0^{3/2}$ [15]. As this volume grows, so does the yield. However, the largest contribution to the yield after the saturation intensity come from those intensities with the highest ionization probability.

One of the effects of using regularization is that the resulting yield $\bar{\boldsymbol{Y}}$ is smoother than the original data. This provides more stability to the retrieved probability $\bar{\boldsymbol{P}}$. Increasing the regularization parameter β strengthens the regularization and minimizes discontinuities in the derivative of $\bar{\boldsymbol{P}}$. Consequently, we used $\beta = 0.5$. Since $\bar{\boldsymbol{P}}$ is the ionization probability per unit volume, we divide it by the gas density (proportional to pressure) in the laser interaction region to obtain the ionization probability per atom. Electrons from different ion charge states have unique ionization probability functions that approach unity as intensity increases. However, these charge states have different saturation intensities. Hence, the graph of the probability first saturates (approaches 1) at $1.2 \times 10^{14}\,\mathrm{W/cm^2}$ and then reaches a maximum value of 2 at approximately $2.7 \times 10^{14}\,\mathrm{W/cm^2}$ (Fig. 4). This second saturation is primarily attributed to single

ionization of the singly charged xenon ion. The MCP detector cannot distinguish between electrons from different charge states. Therefore, electron yields from both species and, by implication, their probabilities are summed giving a "stair step" appearance. In addition to the deconvolved experimental data, Fig. 4 also shows the results of a Perelomov, Popov and Terent'ev (PPT) tunneling ionization simulation [16]. The red curve is the result of summing the calculated ionization probability of both the Xe^{+} and Xe^{+2} ions, whereas the blue curve exclusively represents the Xe^{+2} ionization probability.

Even though the signal shows significant noise, DDAR still recovers the probability. Multiple ionization of Xe has been measured by other groups using ion but not electron detection as in this experiment and compares favorably with our results [1]. The counting electronics naturally groups the electrons according to when they arrive or by their TOF. By transforming this time-series into an energy spectrum and applying DDAR to the yield rates for each electron energy the intensity-resolved (volume independent) energy spectra are obtained. One such spectrum is plotted in Fig. 5.

For the following discussion of features in the ATI spectra see Fig. 5. The first plateau between 0 and 8 eV is the result of "direct" electrons that do not scatter off the parent ion after being ionized. These electrons have a classical cutoff energy of $2U_p$, where U_p is the ponderomotive energy of the laser field [17]. In this low energy region, resonantly enhanced multi-photon ionization (REMPI) is expected to dominate the ATI peak structure (inset) [18]. The second plateau between 12 and 25 eV is dominated by

the interference of electrons which follow different quantum trajectories and are freed with an initially near zero velocity by either tunneling ionization or resonant multiphoton ionization at a channel closing [19]. This ionization mechanism makes the second plateau important also for the study of high harmonic generation [21]. As electrons are accelerated by the electric field, the different quantum paths of electrons with equal momenta can constructively interfere with each other leading to an enhancement in the ionization yield [19,20]. The third plateau, which ranges from 30 to 50 eV, corresponds to elastic backscattering of the electron off the parent ion. This plateau has a cutoff energy of $10.007U_p$ due to the maximum classical energy that a backscattered electron can have [17].

In Fig. 5, the experimental data shows a $10U_p$ value of $\approx$40 eV, which is smaller than that of the deconvolution ($\approx$45 eV). This can be explained by the fact that the peak intensity for each of our Gaussian beams has the smallest three dimensional volume. In our case, we can verify this explicitly by calculating the volume elements of the beams at each peak intensity (Eq. (5)). Figure 6 shows density plots of the ATI spectra as a function of the electron energy (horizontal axis) and laser intensity (vertical axis). The dotted curves drawn on top of the density plots are the $2U_p$ and $10U_p$ cutoff energies calculated from the formula:

$$U_p[\mathrm{eV}] = 9.33\times10^{-14} I_0[\mathrm{W/cm^2}]\lambda^2[\mu\mathrm{m}^2], \tag{9}$$

where λ is the center wavelength in micrometers, I_0 is the intensity in $\mathrm{W/cm^2}$ and the resulting ponderomotive energy has units of eV. For our raw experimental data (Fig. 6(a)), the measured $2U_p$ and $10U_p$ values for each intensity were smaller than values calculated with the DDAR algorithm. This discrepancy could not be removed by adjusting the intensity calibration by a scaling factor. The deconvolution however gives good agreement with the calculated cutoff energies (Fig. 6(b)). So even though the ionization probability is in general higher for larger intensities, the ionization contributions from intensities slightly lower than the peak value can significantly change the spectrum due to their larger volumes. This is important, because it means that the peak intensity and energy of a laser pulse cannot be calculated directly from volume integrated data using the cutoff energies of the spectrum. It should also be noted that none of the spectra from the set of raw data show as much contrast in the ATI peaks as the deconvoluted energy spectra.

V. CONCLUSION

The volume integration in the laser focus reduces the intensity resolution of an experimental measurement. Therefore, we developed a discrete deconvolution and regularization (DDAR) algorithm and applied it to the xenon photoelectron yield to obtain ionization probabilities and intensity-resolved ATI spectra. Our results show for the first time that both single and double ionization probabilities can be retrieved by inverting the electron yield with DDAR. The retrieved Xe^+ ATI spectrum showed sharper peaks throughout the entire energy range compared to the directly measured one.

The $2U_p$ plateau region, where femtosecond pulse ionization from Rydberg states is known to dominate the spectrum, also shows increased contrast after application of the algorithm.

Applying the DDAR algorithm also recovered $2U_p$ and $10U_p$ cutoff energies that are in excellent agreement with theory while the experimental data is not. In the latter, intensities that are below the peak intensity can dominate the ATI spectrum due to their much larger differential volumes. Consequently, this leads to a discrepancy between the intensity predicted from the $10U_p$ cutoff energy and the actual peak intensity. This discrepancy cannot be removed by rescaling the intensity calibration by a multiplicative factor. Therefore, we found that the unwanted volume averaging effect can lead to an underestimation of the $10U_p$ cutoff energy (and this discrepancy grows with increasing intensity) by as much as 30%.

APPENDIX A: ONE-DIMENSIONAL ILLUSTRATION OF THE DECONVOLUTION ALGORITHM

As an example, let us consider a one dimensional case when an experiment is performed at two $(N=2)$ different laser peak intensities, $I_1 > I_2$, and the volume elements are $V_{1,1}$, $V_{1,2}$ and $V_{2,2}$ (see Fig. A1). Using Eq. (3), the measured ion count rates for beams (a) and (b) in Fig. A1 are then approximated respectively by:

$$Y(I_1) = V_{1,2}P(I_2) + V_{1,1}P(I_1), \tag{A1}$$

$$Y(I_2) = V_{2,2} P(I_2). \tag{A2}$$

Since the quantities $Y(I_1)$ and $Y(I_2)$ are measured, and $V_{1,1}$, $V_{1,2}$ and $V_{2,2}$ are known from the focal geometry, it is purely a mathematical exercise to solve Eqs. (A1) and (A2) for $P(I_1)$ and $P(I_2)$:

$$P(I_1) = \frac{1}{V_{1,1}} \left(Y(I_1) - \frac{V_{1,2}}{V_{2,2}} Y(I_2) \right) \tag{A3}$$

$$P(I_2) = \frac{Y(I_2)}{V_{2,2}}. \tag{A4}$$

For the general case of N different laser peak intensities, Eq. (3) produces a system of linear equations:

$$\begin{pmatrix} V_{1,1} & V_{1,2} & \cdots & V_{1,N} \\ 0 & V_{2,2} & \cdots & V_{2,N} \\ \vdots & \cdots & \ddots & \vdots \\ 0 & 0 & \cdots & V_{N,N} \end{pmatrix} \begin{pmatrix} P(I_1) \\ P(I_2) \\ \vdots \\ P(I_N) \end{pmatrix} = \begin{pmatrix} Y(I_1) \\ Y(I_2) \\ \vdots \\ Y(I_N) \end{pmatrix} \tag{A5}$$

or $\hat{V} \cdot \boldsymbol{P} = \boldsymbol{Y}$ where $\hat{V}$ denotes the differential volume matrix, $\boldsymbol{P}$ is the probability array and $\boldsymbol{Y}$ is the signal yield array. To find the probability $\boldsymbol{P}$ we multiply both sides of Eq. (A 5) by the inverse volume matrix $\hat{V}^{-1}$ to obtain:

$$\boldsymbol{P} = \hat{V}^{-1} \cdot \boldsymbol{Y}. \tag{A6}$$

In general, volume matrix encodes the experimental setup into the deconvolution algorithm. It is implicitly dependent on the optical elements in the beam path. Therefore, by computing the appropriate volume matrix elements, the algorithm Eq. (A6) can be

used to deconvolve data from experiments using a variety of laser beam modes (Gaussian, Laguerre Gaussian, Hermite Gaussian, Bessel, etc…).

APPENDIX B: PROCEDURE FOR REGULARIZATION ALGORITHM

In practice the inversion of Eq. (A6) is notoriously unstable, and it is common to remove statistical outliers from the data to improve the algorithm's stability. Here we employ an L2 norm modification of the variation minimization algorithm proposed by Le et. al. [13] and expanded by Chartrand and Wohlberg [14]. Generally, L2 regularization involves the minimization of the dot product $|\boldsymbol{A}|^2$ of a vector $\boldsymbol{A}$, whereas L1 regularization refers to the minimization of the absolute value $|\boldsymbol{A}|$. For convenience of notation we will represent the ionization yields and probabilities in the following way:

$$Y_n \equiv Y(I_n),\ P_s \equiv P(I_s). \tag{B1}$$

From Bayes' theorem, the probability of having a statistical mean $\bar{Y}_n$ given that we measure a yield Y_n can be expressed as:

$$Pr\left(\bar{Y}_n \middle| Y_n\right) = \frac{Pr\left(Y_n \middle| \bar{Y}_n\right) Pr\left(\bar{Y}_n\right)}{Pr\left(Y_n\right)}, \tag{B2}$$

where $Pr(B)$ is the probability of obtaining B and $Pr(A|B)$ is the probability of obtaining A given that we know B. Since Y_n, the measurement, cannot be changed, maximizing $Pr\left(\bar{Y}_n \middle| Y_n\right)$ requires ascertaining the appropriate $\bar{Y}_n$. Maximizing $Pr\left(\bar{Y}_n \middle| Y_n\right)$

is therefore equivalent to maximizing $Pr\left(Y_n \middle| \bar{Y}_n\right) Pr\left(\bar{Y}_n\right)$. The data Y_n is measured over a fixed interval of time satisfying Poisson statistics. Therefore the probability of measuring Y_n, provided a mean $\bar{Y}_n$, is given by the Poisson probability mass function:

$$Pr\left(Y_n \middle| \bar{Y}_n\right) = \frac{e^{-\bar{Y}_n} \bar{Y}_n^{Y_n}}{Y_n!}. \tag{B3}$$

The regularization of the data is typically introduced through the probability $Pr\left(\bar{Y}_n\right)$. However, it is more useful to regularize the output of the deconvolution algorithm $\bar{\boldsymbol{P}}$, since this is where the propagated error tends to be the largest. Consequently, the function $Pr\left(\bar{Y}_n\right)$ is replaced by a suitable function $Pr\left(\bar{P}_n\right)$. This function must be chosen based upon experimental constraints. Assuming the derivative of the ionization probability to be continuous, we chose:

$$Pr\left(\bar{P}_n\right) = exp\left(-\beta\left(\nabla_{n,s} \bar{P}_s\right)^2\right), \tag{B4}$$

where the local derivative,

$$\left|\nabla_{n,s} \bar{P}_s\right| \approx \left|\frac{\partial \bar{P}}{\partial I}\right|_n, \tag{B5}$$

is with respect to the array variable I, and β is the regularization parameter. The choice of β is discussed in Section IV. Since we ultimately seek the statistical mean of the ionization probability $\bar{\boldsymbol{P}}$, we eliminate the yield mean by the substitution

$$\bar{\boldsymbol{Y}} \to \hat{V}\bar{\boldsymbol{P}}. \tag{B6}$$

We can now maximize Eq. (B2) by minimizing the negative logarithm:

$$\begin{aligned} -\log\left(Pr\left(Y_n \middle| \bar{Y}_n\right) Pr\left(\bar{P}_n\right)\right) &= \bar{Y}_n - Y_n \log\left(\bar{Y}_n\right) + \log\left(Y_n!\right) + \beta\left(\bar{Y}_n\right)^2 \\ &= V_{n,s}\bar{P}_s - Y_n \log\left(V_{n,s}\bar{P}_s\right) + \log\left(Y_n!\right) + \beta\left(\nabla_{n,s}\bar{P}_s\right)^2. \end{aligned} \tag{B7}$$

Equation (B7) can be viewed as a mechanical action, from which we derive the Euler-Lagrange equation with respect to the variables $\bar{P}_s$ and $\nabla_{n,s}\bar{P}_s$, resulting in

$$\hat{V}^T \frac{\hat{V}\bar{\boldsymbol{P}} - \boldsymbol{Y}}{\left|\hat{V}\bar{\boldsymbol{P}}\right|} - 2\beta\hat{\nabla}^2\bar{\boldsymbol{P}} = 0. \tag{B8}$$

It should be noted that in Eq. (B8), $\hat{M} \equiv \left|\hat{V}\bar{\boldsymbol{P}}\right|$ is a diagonal matrix whose elements are:

$$M_{n,m} = \begin{cases} V_{n,s}\bar{P}_s \to n = m \\ 0 \to n \neq m \end{cases}. \tag{B9}$$

This $\hat{M}$ has the general effect of rescaling the regularization parameter $\beta\left(I_n\right) = \beta M_{n,n}$ to accommodate the variation in the Poisson noise. Because $\hat{M}$ is a function of $\bar{\boldsymbol{P}}$ (and $\bar{\boldsymbol{P}}$ is the desired quantity), $\hat{M}$ will have to be approximated through an iterative process. If the experimental data is taken such that the measurement approximates the statistical mean, $\boldsymbol{Y} \approx \bar{\boldsymbol{Y}} = \hat{V}\bar{\boldsymbol{P}}$, we can approximate Eq. (B9) by setting the initial value $\hat{M}_0 = \left|\boldsymbol{Y}\right|$ and solving for the probability $\bar{\boldsymbol{P}}_i$:

$$\bar{\boldsymbol{P}}_i = \left(\hat{V}^T\hat{V} - 2\beta\hat{M}_i\hat{\nabla}^2\right)^{-1}\hat{V}^T\boldsymbol{Y}\,, \tag{B10}$$

$$\hat{M}_{i+1} = \left|\hat{V}\bar{\boldsymbol{P}}_i\right|. \tag{B11}$$

Equations (B10) and (B11) are iterated until convergence ($\left|\bar{\boldsymbol{P}}_i - \bar{\boldsymbol{P}}_{i+1}\right| < \left|\bar{\boldsymbol{P}}_{i+1}\right|/10^4$) is obtained for every element of the vector $\bar{\boldsymbol{P}}_{i+1}$. For our data, only two iterations were needed for convergence. In Eq. (B11), the initial $\hat{M}_i$ ($i = 0$) is the diagonal matrix of the measured yields

$$\left|\boldsymbol{Y}\right| = \begin{pmatrix} \left|Y_1\right| & 0 & \cdots & 0 \\ 0 & \left|Y_2\right| & 0 & \vdots \\ \vdots & 0 & \ddots & 0 \\ 0 & 0 & 0 & \left|Y_n\right| \end{pmatrix}, \tag{B12}$$

and $\hat{\nabla}^2$ is the second derivative matrix. We found the second derivative by multiplying two first derivative matrices defined by

$$\hat{\nabla} = \frac{1}{\Delta I}\begin{pmatrix} 1 & -1 & 0 & . & 0 \\ 0 & 1 & -1 & 0 & . \\ . & 0 & 1 & . & 0 \\ . & . & 0 & . & -1 \\ 0 & . & . & 0 & 1 \end{pmatrix}. \tag{B13}$$

In general, the intensity spacing $\Delta I = I_i - I_{i+1}$ is not constant and should be calculated for each row of the derivative matrix. We refer to the initialization step along with the

iteration of Eqs. (B10, B11) and the convergence criterion as the discrete deconvolution and regularization (DDAR) algorithm.

ACKNOWLEDGMENTS

This work was funded by the Robert A. Welch Foundation Grant No. A1546 and the Qatar Foundation under the grants NPRP 5 - 994 - 1 – 172 and NPRP 6 - 465 - 1 - 091.

REFERENCES

[1] S. Larochelle, A. Talebpour, and S. L. Chin, J. Phys. B: At. Mol. Opt. Phys. **31**, 1201 (1998)

[2] P. Lambropoulos, AIP Conf. Proc., **275**, 499 (1993).

[3] J. Strohaber and C. Uiterwaal, Phys. Rev. Lett. **100**, 023002 (2008).

[4] K. J. Schafer and K. C. Kulander, Phys. Rev. A, **42**, 5794 (1990).

[5] E. Cormier and P. Lambropoulos, J. Phys. B, **30**, 77 (1997).

[6] P. Hansch and L. D. Van Woerkom, Opt. Lett., **21**, 1286 (1996).

[7] M. A.Walker, L. D. Van Woerkom, and P. Hansch, Phys. Rev. A, **57**, R701 (1998).

[8] W. A. Bryan, S. L. Stebbings, E. M. English, T. R. Goodworth, W. R. Newell, J. McKenna, et al. Phys. Rev. A, **73**, 013407 (2006).

[9] T. R. J. Goodworth, W. A. Bryan, I. D. Williams, and W. R. Newell, J. Phys. B **38**, 3083 (2005).

[10] M. Schultze, B. Bergues, H. Schröder, F. Krausz, and K. L. Kompa, New J. Phys., **13**, 033001 (2011).

[11] J. Strohaber, A. A. Kolomenskii, H. A. Schuessler, Phys. Rev. A, **82**, 013403 (2010).

[12] R. W. Boyd, *Nonlinear Optics* (Academic Press, Waltham, MA, 2008).

[13] T. Le, R. Chartrand and T. Asaki, JMIV, **27**, 257 (2007).

[14] R. Chartrand and Wohlberg, B., Presented at the IEEE ICASSP, Dallas, TX, USA, (2010).

[15] S. Speiser and J. Jortner, Chem. Phys. Lett. **44**, 399 (1976).

[16] A. M. Perelomov, V. S. Popov, and M. V. Terent'ev, Zh. Eksp. Teor. Fiz. **50**, 1393 (1966) [Sov. Phys. JETP **23**, 924 (1966)].

[17] G. G. Paulus, W. Becker, W. Nicklich, H. Walther, J. Phys. B, **27**, L703 (1994).

[18] McIlrath, T.J.,Freeman, R.R., Cooke, W. E. and Woerkom, L.D. Phys. Rev. A **40**, 2770. (1989).

[19] G. G. Paulus, F. Grasbon, H. Walther, R. Kopold, and W. Becker, Phys. Rev. A, **64**, 021401(R). (2001).

[20] G. G. Paulus, F. Grasbon, A. Dreischuh, H. Walther, R. Kopold and W. Becker Phys. Rev. Lett. **84**, 3791–3794 (2000).

[21] R. Kopold, W. Becker, M. Kleber and G. G. Paulus, J. Phys. B: At. Mol. Opt. Phys. **35** 217 (2002).

FIGURE CAPTIONS

FIG. 1. (Color online) An example schematic in one dimension showing how volume elements are related to peak intensities. Here the total number of experiments is $N = 3$. The boundary of each volume (horizontal) is set by intensities δI and I_3. δI is a free parameter that provides an outer boundary for the calculation of the volume elements. The central blue region represents $V_{3,3}$, the sandwiched red regions are $V_{2,3}$ and the outer gold regions are $V_{1,3}$. Each of these three volumes correspond to the same ionization probability $P(I_3)$.

FIG. 2. (Color online) Experimental setup: M, mirror; WP, half wave plate; PD, photo diode; PBC, polarizing beam-splitter cube; L, lens; MCP, chevron microchannel plate; PM, power meter.

FIG. 3. (Color online) The experimentally measured electron yield **Y** on a Log-Log plot. Two slopes are plotted showing the intensity dependence: a slope of 5 (solid line), and a slope of 3/2 (dashed line). The change in slope occurs slightly above the saturation intensity $I_{sat} = 1.2 \times 10^{14}\,\mathrm{W/cm^2}$.

FIG. 4. (Color online) Recovered electron probability on a Log-Log plot (dotted line). The red curve is a PPT theory simulation of the xenon probability for electron yields for Xe^{+1} and Xe^{+2}. The blue curve shows the simulation of the electron yield probability for Xe^{+2} electrons alone. The deconvolution diverges at the high intensity end point.

FIG. 5. (Color online) Intensity-resolved ATI energy spectra at 8.7×10^{13} W/cm^2 of electrons per laser pulse. The red curve is the measured data prior to being deconvolved. The deconvolution shows more pronounced features. The inset shows the $2U_p$ low energy region of the same data. REMPI peaks can be seen at energies less than 4 eV.

FIG. 6. (Color online) Density plots of the ATI spectra as a function of energy (horizontal-axis) and intensity (vertical-axis). In both graphs the $2U_p$ and $10U_p$ cutoff energies for each intensity are denoted by the dotted black and white lines, respectively. (a) The density plot of the experimental data shows a discrepency between the calculated cutoff energies and the measured ones. (b) The deconvolution of the experimental data recovers the calculated cutoff energies and suggests a better agreement with theory [17].

FIG. A1. (Color online) A one dimensional illustration of Gaussian beams showing the relationship between the volume elements ($V_{1,1}$, $V_{1,2}$, $V_{2,2}$) and their respective probabilities ($P(I_1)$, $P(I_2)$). Regions within the beams with an ionization probability of $P(I_1)$ are colored blue, while regions with probability $P(I_2)$ are colored red. Beam (a) is represented by Eq. (A2). The differential volume of the red region is denoted by $V_{2,2}$. Beam (b) is represented by Eq. (A1). Here the differential volume of the red region is denoted by $V_{1,2}$ and that of the blue region is denoted by $V_{1,1}$. The gold wings of each beam are neglected in Eqs. (A1) and (A2).

FIGURES

Fig. 1

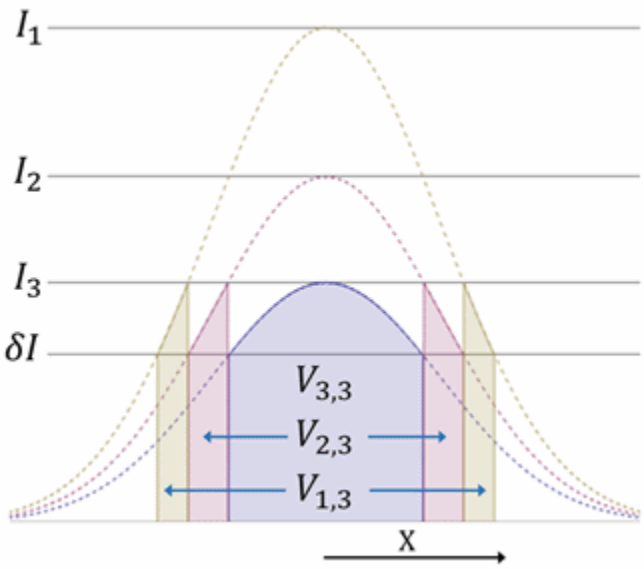

Fig. 2

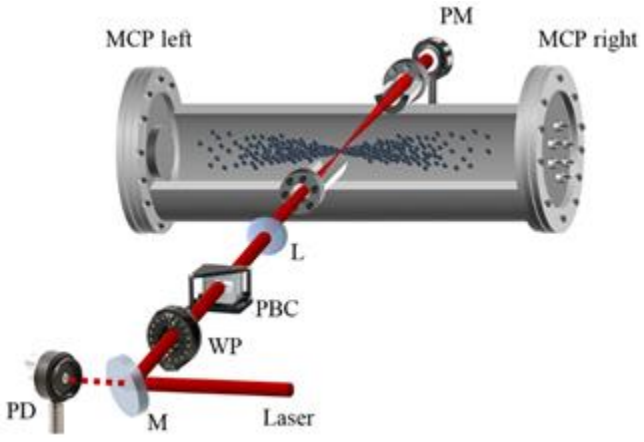

Fig. 3

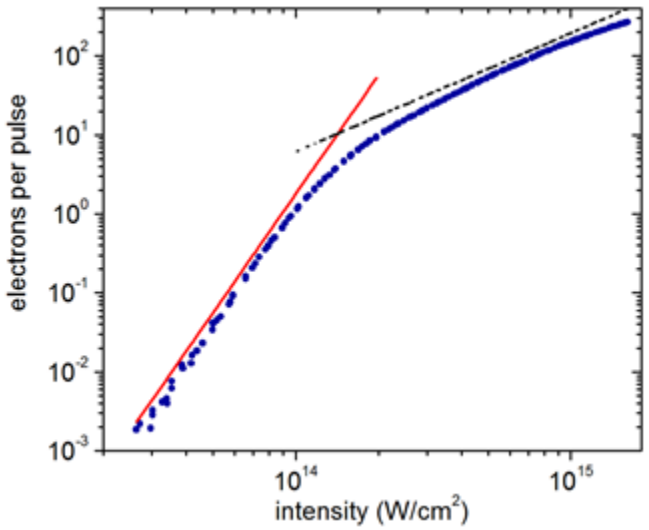
electrons per pulse
10^{2}
10^{1}
10^{0}
10^{-1}
10^{-2}
10^{-3}
10^{14}
10^{15}
intensity (W/cm^2)

Fig. 4

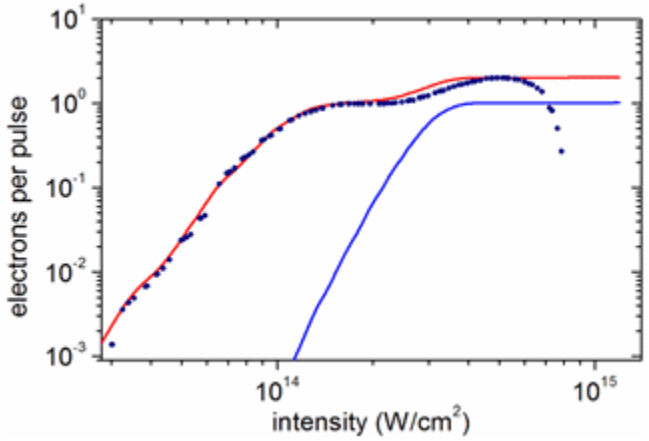
electrons per pulse
10^{1}
10^{0}
10^{-1}
10^{-2}
10^{-3}
10^{14}
10^{15}
intensity (W/cm^2)

Fig. 5

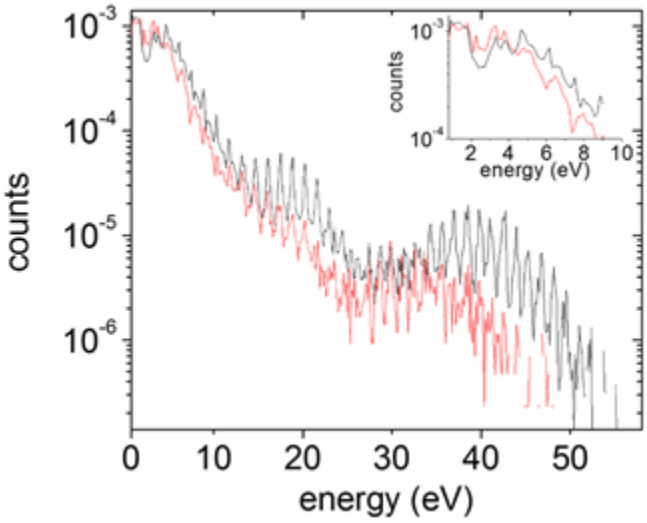
counts
energy (eV)
10^-3
10^-4
10^-5
10^-6
0
10
20
30
40
50
counts
energy (eV)
2
4
6
8
10

Fig. 6

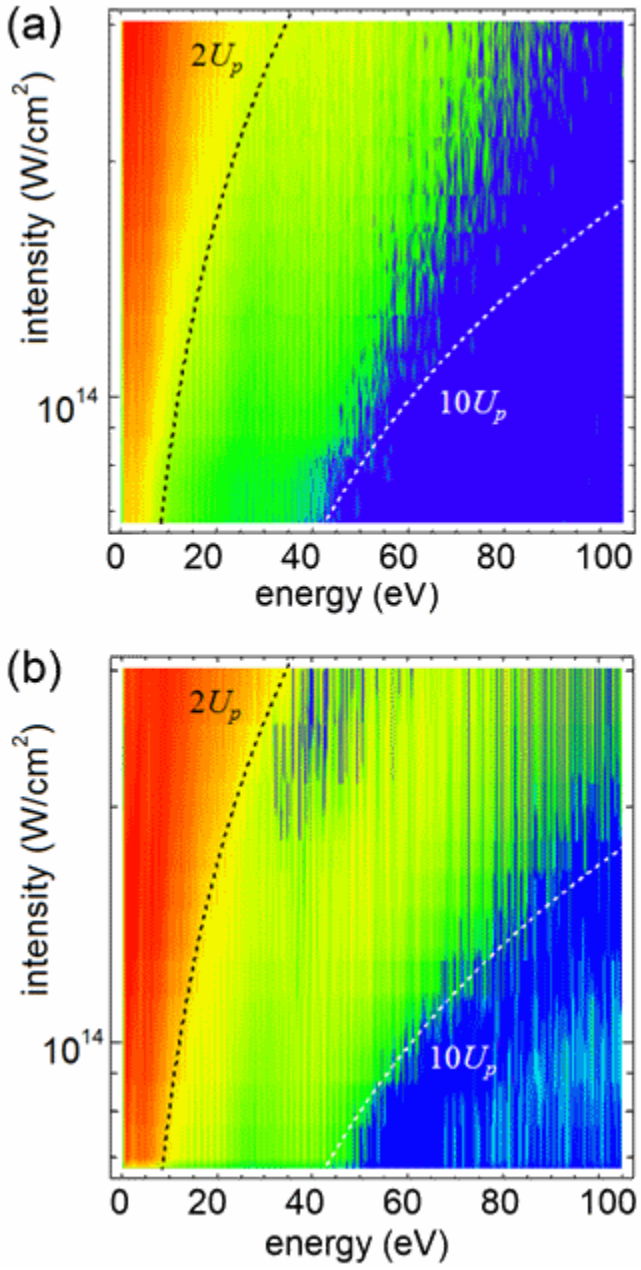
(a)
intensity (W/cm^2)
10^{14}
$2U_p$
$10U_p$
0
20
40
60
80
100
energy (eV)
(b)
intensity (W/cm^2)
10^{14}
$2U_p$
$10U_p$
0
20
40
60
80
100
energy (eV)

Fig. A1